

Identification of double b -hadron jets from
gluon-splitting with the ATLAS Detector

María Laura González Silva

Doctoral Thesis in Physics

Physics Department

University of Buenos Aires

November 2012



UNIVERSIDAD DE BUENOS AIRES

Facultad de Ciencias Exactas y Naturales

Departamento de Física

**Identificación de jets con hadrones b producidos por
desdoblamiento de gluones con el detector ATLAS.**

Trabajo de Tesis para optar por el título de
Doctor de la Universidad de Buenos Aires en el área Ciencias Físicas

por **María Laura González Silva**

Director de Tesis: Dr. Ricardo Piegaia

Lugar de Trabajo: Departamento de Física

Buenos Aires, Noviembre 2012

Agradecimientos

Quiero agradecer a mi director, Ricardo Piegaia, por darme la oportunidad de trabajar en el proyecto ATLAS, por su dedicación y su enseñanza constante; y a mis compañeros de grupo, Gastón Romeo, Gustavo Otero y Garzón, Hernán Reisin y Sabrina Sacerdoti por el trabajo compartido y por brindarme su amistad a lo largo de estos años. Quiero agradecer a Ariel Schwartzman por darnos este análisis, por su caudal inagotable de ideas y por su generosidad y la de todo su equipo. Agradezco al Laboratorio CERN, al Experimento ATLAS, a los programas HELEN y e-Planet, al CONICET y al Fundación Exactas por hacer posible la realización de esta tesis.

Quiero agradecer el apoyo de mis compañeros de la carrera, especialmente a mis amigos Cecilia, Tomás y Leandro. Quiero agradecer también a mis compañeros de grupo y oficina, Javier, Yann, Pablo, y Orel por estar siempre dispuestos a darme una mano. Quiero agradecer a los amigos que hice a lo largo de estos años en mis visitas al Laboratorio CERN, Laura, Bárbara, Teresa, Manouk, Lucile, Alex, Olivier, Bruno y Haris; y a mis colegas y amigos de la Universidad de La Plata, Fernando, Martín y Xabier, por los maravillosos momentos compartidos.

Agradezco profundamente a mis amigos y a toda mi familia por su apoyo y aliento; y de manera especial a mamá y a Juan, por comprenderme y acompañarme en todo. A ellos les dedico esta tesis.

Identificación de jets con hadrones b producidos por desdoblamiento de gluones con el detector ATLAS.

Resumen

En esta tesis se presenta un estudio de la subestructura de jets que contienen hadrones b con el propósito de distinguir entre jets- b genuinos, donde el quark b se origina a nivel de elemento de matriz (por ejemplo, en decaimientos de top, W, o Higgs) y jets- b producidos en la lluvia partónica de QCD, por el desdoblamiento de un gluón en un quark y un antiquark b cercanos entre sí. La posibilidad de rechazar jets- b producidos por gluones es importante para reducir el fondo de QCD en análisis de física dentro del Modelo Estándar, y en la búsqueda de canales de nueva física que involucran quarks b en el estado final. A tal efecto, se diseñó una técnica de separación que explota las diferencias cinemáticas y topológicas entre ambos tipos de jets- b . Esta se basa en observables sensibles a la estructura interna de los jets, construídos a partir de trazas asociadas a éstos y combinados en un análisis de multivariable. En eventos simulados, el algoritmo rechaza 95% (50%) de jets con dos hadrones b mientras que retiene el 50% (90%) de los jets- b genuinos, aunque los valores exactos dependen de p_T , el momento transverso del jet. El método desarrollado se aplica para medir la fracción de jets con dos hadrones b en función del p_T del jet, con $4,7 \text{ fb}^{-1}$ de datos de colisiones pp a $\sqrt{s} = 7 \text{ TeV}$, recogidos por el experimento ATLAS en el Gran Colisionador de Hadrones en 2011.

Palabras clave: Experimento ATLAS, Jets, Subestructura de Jets, QCD, Producción de jets b , Etiquetado de Jets b .

Identification of double b -hadron jets from gluon-splitting with the ATLAS Detector.

Abstract

This thesis presents a study of the substructure of jets containing b -hadrons with the purpose of distinguishing between “single” b -jets, where the b -quark originates at the matrix-element level of a physical process (e.g. top, W or Higgs decay) and “merged” b -jets, produced in the parton shower QCD splitting of a gluon into a collimated b quark-antiquark pair. The ability to reject b -jets from gluon splitting is important to reduce the QCD background in Standard Model analyses and in new physics searches that rely on b -quarks in the final state. A separation technique has been designed that exploits the kinematic and topological differences between both kinds of b -jets using track-based jet shape and jet substructure variables combined in a multivariate likelihood analysis. In simulated events, the algorithm rejects 95% (50%) of merged b -jets while retaining 50% (90%) of the single b -jets, although the exact values depend on p_T , the jet transverse momentum. The method developed is applied to measure the fraction of double b -hadron jets as a function of jet p_T , using 4.7 fb^{-1} of pp collision data at $\sqrt{s} = 7 \text{ TeV}$ collected by the ATLAS experiment at the Large Hadron Collider in 2011.

Keywords: ATLAS Experiment, Jets, Jet Substructure, b -jet Production, QCD, Gluon Splitting, b -tagging.

Contents

| | |
|---|-----------|
| 1 The ATLAS Detector at the LHC | 2 |
| 1.1 The Large Hadron Collider | 2 |
| 1.1.1 Luminosity and pile-up | 6 |
| 1.2 The ATLAS Detector | 9 |
| 1.2.1 Inner Tracking System | 12 |
| 1.2.2 The Calorimeter System | 15 |
| 1.2.3 The Muon System | 22 |
| 1.2.4 Forward Detectors | 24 |
| 1.2.5 Trigger and Data Adquisition System | 24 |
| 1.2.6 ATLAS performance and data quality | 26 |
| 2 Event reconstruction and <i>b</i>-Tagging | 29 |
| 2.1 Jet reconstruction and calibration | 29 |
| 2.2 Reconstruction of charged particle tracks | 40 |
| 2.3 Vertex reconstruction | 42 |
| 2.4 <i>b</i> -jet Tagging | 43 |
| 2.4.1 <i>b</i> -tagging algorithms | 47 |
| 2.4.2 <i>b</i> -tagging calibration | 55 |

Chapter 1

The ATLAS Detector at the LHC

1.1 The Large Hadron Collider

The Large Hadron Collider (LHC) [1] is a proton-proton (pp) synchrotron located in the previous Large Electron Positron (LEP) collider tunnel at CERN Laboratory, just outside the city of Geneva (Switzerland), approximately 100 m underground. It is designed to collide bunches of up to $\sim 10^{11}$ protons every 25 ns at a center-of-mass energy of 14 TeV (seven times the 2 TeV reached by the Tevatron accelerator at Fermilab Laboratory, in Chicago).

The experiments analyzing the collisions produced by the LHC are distributed around the 27 km ring at the various interaction points. The ATLAS experiment is located at Point 1, which is closest to the main CERN site. Point 5 houses the other general purpose detector, CMS. ALICE and LHCb experiments are located at Point 2 and Point 8, respectively. The former is designed to investigate heavy ion collisions; the latter, to investigate rare decays of b -mesons. The layout of these four experiments along the LHC ring is shown in Fig. 1.1.

Proton beams are formed, before insertion into the main LHC ring, using

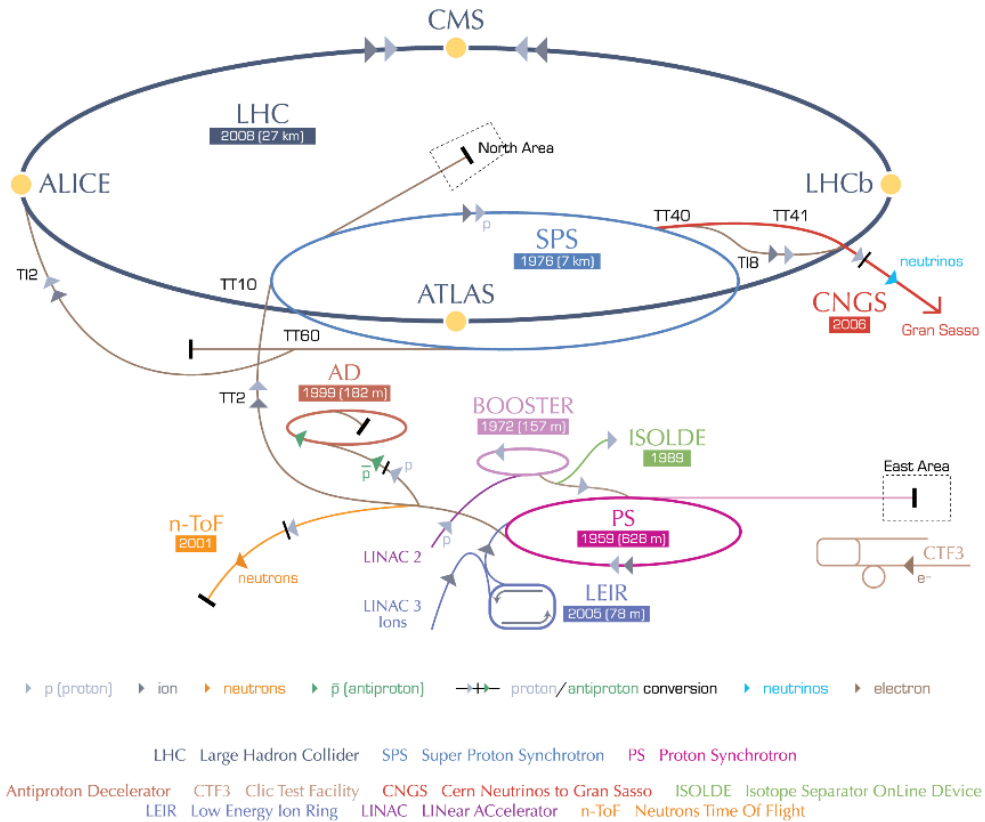


Figure 1.1: The CERN accelerator complex, showing the injection system, along with each component's date of construction, and the placement of the four main experiments.

a succession of smaller machines with increasingly higher energies, as shown in Fig. 1.1. The chain begins as protons are injected into the PS Booster (PSB) at an energy of 50 MeV from Linac2. The booster accelerates them to 1.4 GeV. The beam is then fed to the Proton Synchrotron (PS) where it is accelerated to 25 GeV. At design strength, the bunch structure, known as a bunch train, contains 72 bunches of protons upon entry to the Super Proton Synchrotron (SPS). The SPS accumulates up to four fills of 72 bunches from the PS and accelerates them to 450 GeV, with a bunch spacing of ~ 25 ns. They are finally transferred to the LHC (both in a clockwise and an anticlockwise direction) where they are accelerated for 20 minutes to their nominal energy of 7 TeV. Beams will circulate for many hours inside the LHC beam pipes under normal operating conditions.

The bunch structure is a direct consequence of a radio frequency (RF) acceleration scheme used to attain the desired high proton beam energy. In RF acceleration, particles travel through a series of time-varying electrical fields and they can only be accelerated when the RF field has the correct orientation when particles pass through an accelerating cavity, which happens at well specified moments during an RF cycle. The result of a sequence of RF accelerations is several bunches of protons. It is important to note that when we speak about “beams” we refer to many bunches of protons separated by some uniform distance. Increasing the number of bunches is one of the ways to increase luminosity in a machine (more about luminosity in subsection 1.1.1). At designed beam intensity, when the bunches cross, there will be a maximum of about 20 collisions.

A large magnetic field is needed to guide and maintain the beam particles in their circular orbit. The needed field is achieved using superconducting electromagnets built from NbTi coils that operate in a superconducting

state, efficiently conducting electricity without resistance or loss of energy. The currents through the coils produce magnetic fields perpendicular to the direction of motion of the protons that deflect the protons into their orbits. The whole magnetic system comprises 1232 dipole magnets of 15 m length which are used to bend the beams, and 392 quadrupole magnets, each 5-7 m long, to focus the beams. At a peak beam energy of 7 TeV, the dipoles need to produce an 8.33 T magnetic field, requiring a current of ~ 12 kA. In order to deliver the current densities and magnetic field required for 7 TeV proton beams, the magnets are kept at 1.9 K by circulating superfluid helium.

The first pp collisions produced by the LHC occurred on November 23 2009, at the SPS extraction energy of 450 GeV per beam. Very quickly after, on December 8, ATLAS and CMS detectors started recording data at energy of 2.36 TeV. By this time the LHC became the highest energy accelerator in the world. During this period, bunch intensities were limited by machine-protection considerations to 1.5×10^{10} protons.

In February 2010, the LHC was commissioned once more with 450 GeV beams, and a series of tests were performed to ensure that the magnet systems could operate safely at the currents necessary to control 3.5 TeV beams. This was followed by the very first collisions at 7 TeV center-of-mass energy on March 30. During the 2010 run the beam parameters were tuned (the beam widths squeezed and the number of protons per bunch and the number of bunches in each beam increased) in order to increase the beam intensity. In particular, as the intensity of the beams increased, the mean number of interactions per bunch crossing increased.

The data samples analyzed in this thesis correspond to proton-proton collisions at $\sqrt{s} = 7$ TeV delivered by the LHC and recorded by ATLAS between May and November 2011, with the LHC running with 50 ns bunch

spacing. Table 1.1 summarizes the basic beam parameters expected for design energy and luminosity and the beam parameters as of May 2011. The LHC performance steadily improved during 2011. The average number of interactions per bunch crossing throughout the data-taking period considered rapidly increased approximately from ~ 3 to 8 until (northern hemisphere) summer 2011, with a global average for this period of ≈ 6 . Starting in August 2011 and lasting through the end of the proton run, this number ranged from approximately 5 to 17, with an average of about 12. This evolution is illustrated in Fig. 1.2, which shows the maximum mean number of collisions per beam crossing versus day in 2011.

| Parameter | 2011 runs | Design |
|--|----------------------------------|----------------------|
| Center-of-mass energy [TeV] | 7 | 14 |
| Instantaneous luminosity [$\text{cm}^{-2}\text{s}^{-1}$] | $3.65 \cdot 10^{33}$ (year peak) | 10^{34} |
| Bunches per beam | 38 (May) | 2808 |
| Protons per bunch | 0.8×10^{11} (May) | 1.5×10^{11} |
| Mean interactions per crossing | 6 to 12 (year average) | 23 |

Table 1.1: Summary of beam conditions during the 2011 7 TeV runs and those foreseen at design energy and luminosity.

1.1.1 Luminosity and pile-up

The rate of events produced by the colliding beams depends on the luminosity of the collisions, which is a measure of the number of events per second per unit cross section, typically measured in units cm^2s^{-1} . The number of events of a particular process, then, is given by the product of the integrated luminosity, $\int dt L$, and the cross section of the process, σ_{event} . The

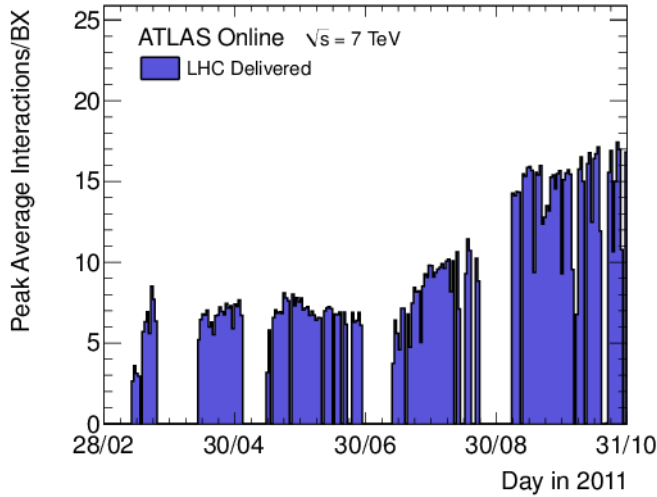


Figure 1.2: The maximum mean number of events per beam crossing versus day in 2011.

integrated luminosities are typically quoted in units of inverse picobarns, $\text{pb}^{-1} = 10^{-36}\text{cm}^2$. In order to measure processes with very little cross sections a very high luminosity is required.

The delivered luminosity can be written as [2]:

$$L = \frac{n_b f_r n_1 n_2}{2\pi \Sigma_x \Sigma_y} \quad (1.1)$$

where n_b is the number of colliding bunch pairs, n_1 and n_2 are the bunch populations (protons per bunch) in beam 1 and beam 2 respectively (together forming the bunch charged product), f_r is the machine revolution frequency, and Σ_x and Σ_y are the width and the height of the proton beams.

The number of protons per bunch, the number of bunches per beam, and the revolution frequency are all set by the beam operators. The widths of the proton beams are measured in a process known as a Van der Meer (*vdm*) scan [3]. In a *vdm* scan, the beams are separated by steps of a known

distance. The collision rate is measured as a function of this separation, and the width of a gaussian fit to the distributions yields the width of the beams in the direction of the separation.

The total integrated luminosities provided by the LHC and recorded by ATLAS in 2011 are shown in Figure 1.3. These events form the dataset analyzed in this thesis. By means of the beam-separation or vM scans, as well as other techniques to measure the bunch charged product, the ATLAS Collaboration has determined that the uncertainty on its luminosity measurement is $\delta L = \pm 3.7\%$. For a complete description of the methods used and the systematic errors evaluated see reference [2].

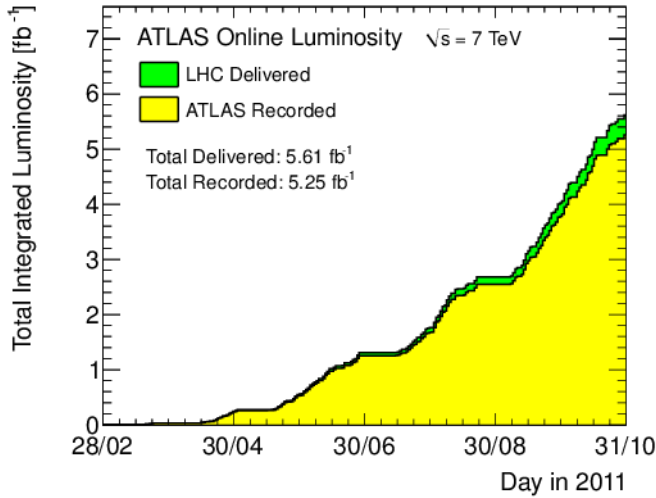


Figure 1.3: Total luminosity delivered by the LHC and recorded by ATLAS during the 2011 $\sqrt{s} = 7$ TeV proton-proton run.

As anticipated, due to the cross-section for interaction and the number of protons per bunch, the possibility to observe multiple pp interactions per bunch crossing increases proportionally. This phenomenon, referred to as “pile-up”, can really occur in two distinct forms. The first form is the pres-

ence of multiple pp collisions (different from the interaction of interest) in the same bunch crossing, referred to as “in-time” pile-up. The second form of pile-up takes place due to electronic integration times within the detector. Certain detector components are actually sensitive to multiple bunch crossings due to the long electronic signals generated in the response to energy depositions or charge collection. One or more pp collisions in a bunch-crossing different from that which produced the collision of interest can then affect the measurement. This form of pile-up is referred to as “out-of-time” pile-up and will become more and more important as the LHC bunch spacing gets closer to the nominal value, 25 ns.

The fraction of events with pile-up increased significatively since the data taking started. The experimental signature of this fact is obtain via the number of reconstructed primary vertices, or NPV. The effect of the event NPV is an important concern for the measurement of jet properties and will be discussed in the next chapters.

1.2 The ATLAS Detector

The ATLAS detector [4] is one of the two general purpose particle detectors built for probing pp collisions at the LHC. As it was described in the previous section, inside the LHC, bunches of up to 10^{11} protons will collide 40 million times per second to provide 14 TeV proton-proton collisions at a nominal luminosity of $10^{34}\text{cm}^{-2}\text{s}^{-1}$. These high interaction rates and energies, as well as the requirements for high precision physics measurements set the standars for the design of the detector. At even 7 TeV center-of-mass energy, the LHC interactions result in high particle multiplicity, requiring fine

detector granularity, and particle production at forward rapidity, requiring large detector angular coverage.

To achieve these performance goals, a design consisting of multiple detector sub-systems with cylindrical symmetry around the incoming beams is used as shown in Fig. 1.4. Closest to the interaction point the inner tracking detector is placed, providing charged particle reconstruction. The magnet configuration comprises a thin superconducting solenoid surrounding the inner detector cavity, and three large superconducting toroids (one barrel and two end-caps) arranged with an eight-fold azimuthal symmetry around the calorimeters. This fundamental choice has driven the design and size (44 m in length and 25 m in height) of the rest of the detector. Outside the solenoid, a calorimeter system performs electron, photon, tau, and jet energy measurements. Finally, the calorimeter is surrounded by the muon spectrometer where an array of muon drift chambers perform muon identification and momentum measurements.

The ATLAS detector coordinate system is used to describe the position of particles as they traverse these subdetectors. It is a right-handed coordinate system, with z pointing along the beam direction, positive x pointing toward the center of the LHC ring, and positive y pointing up. The $x - y$ plane is referred to as the transverse plane, and the z direction as the longitudinal direction. The azimuthal angle ϕ is measured as usual around the beam axis, and the polar angle θ is the angle from the beam axis. The pseudorapidity is defined as $\eta = \ln(\tan(\frac{\theta}{2}))$, regions of low η are referred to as “central”, and regions of high η are referred to as “forward”. The transverse momentum p_T is defined in the $x - y$ plane unless stated otherwise. The distance ΔR in the pseudorapidity-azimuthal angle space is defined as $\Delta R = \sqrt{\Delta\eta^2 + \Delta\phi^2}$.

To meet the extremely high demands that the LHC luminosity places

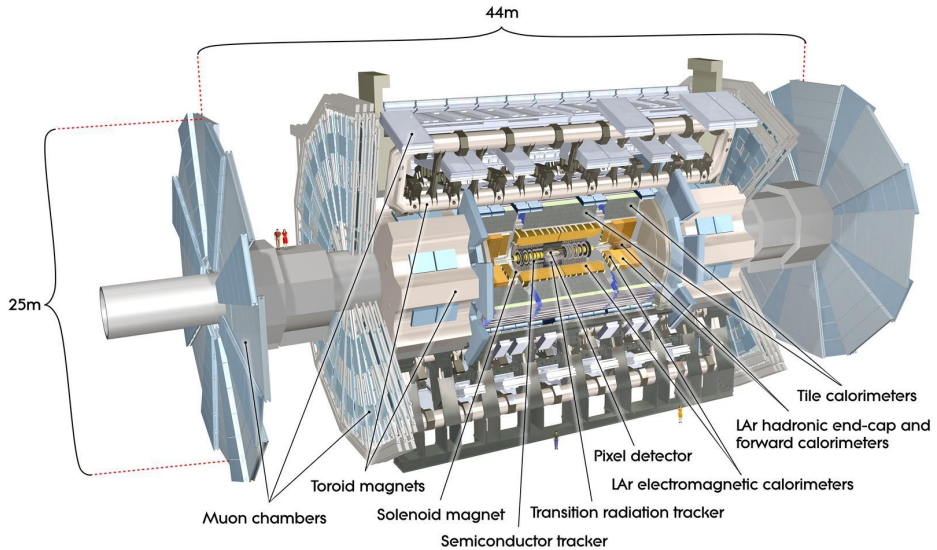


Figure 1.4: The ATLAS Detector.

on the speed with which ATLAS must record data, a dedicated trigger and data acquisition (TDAQ) system is used. The interaction rate at the design luminosity is approximately 1 GHz, while the event data recording, based on technology and resource limitations, is limited to about ~ 200 Hz. This requires a high rejection of minimum-bias processes while maintaining maximum efficiency for the new physics. The Level-1 (L1) trigger system uses a subset of the total detector information to make a decision on whether or not to continue processing an event, reducing the data rate to approximately 75 kHz (limited by the bandwidth of the readout system, which is upgradeable to 100 kHz). The subsequent two levels, collectively known as the high-level trigger (HLT), are the Level-2 (L2) trigger and the Event Filter (EF). They provide the reduction to a final data-taking rate of approximately 200 Hz.

1.2.1 Inner Tracking System

The inner tracking system or Inner Detector (ID) is composed of three sub-detectors: the pixel detector, the semiconductor tracker (SCT) and the transition radiation tracker (TRT). The goal of these three is to provide charged particle trajectory reconstruction and momentum measurements with an overall acceptance in pseudorapidity of $|\eta| < 2.5$ and full ϕ coverage.

The sensors which built this system register signals, referred to as “hits”, in response to the passage of charged particles. The ID is immersed in a 2 T magnetic field, generated by the central solenoid. The positions of the registered hits are combined to form tracks, with the radius of curvature of the tracks (caused by the presence of the magnetic field) providing a measurement of the particle’s transverse momentum. The track reconstruction efficiency ranges from 78% at $p_T^{track} = 500$ MeV to more than 85% above 10 GeV, averaged across the full η coverage [5]. The transverse momentum resolution of $\sigma_{p_T}/p_T = 0.05$ [6] (upper bound) and a transverse impact parameter resolution of $\sim 20 \mu\text{m}$ for high momentum resolution particles in the central η region [7] are primarily achieved through the use of high precision subsystems within the ID.

The pixel detector, SCT, and TRT sensors are arranged on concentric cylinders around the beam axis, known as barrel layers, and on disks perpendicular to the beam at either end of the barrel, known as end-caps. A more complete description of these systems is given below. The overall layout of the inner detector is shown in Fig. 1.5.

The Pixel detector

The pixel detector consists of three concentric barrel layers. The innermost one, the so called “*b*-layer” due to its role in identifying *b*-quarks initiated

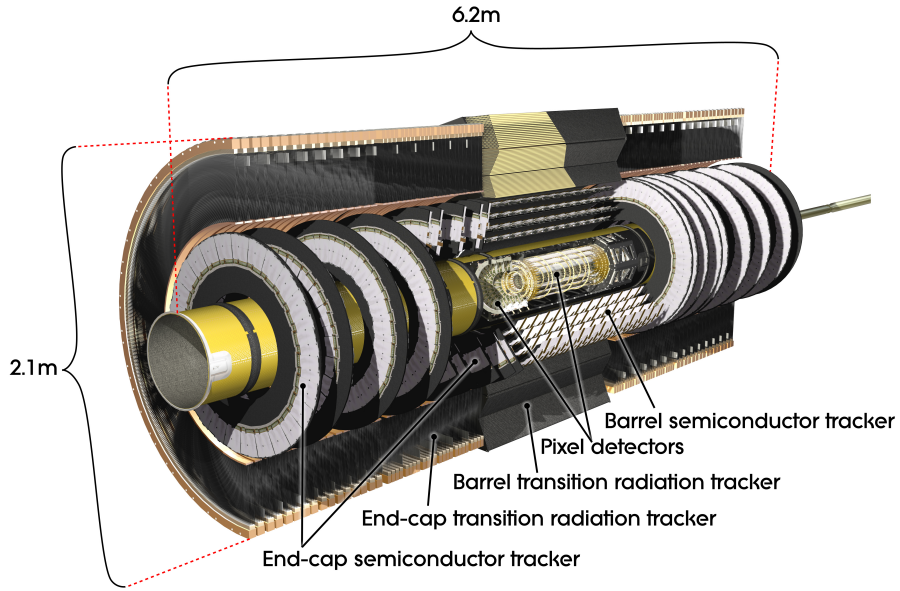


Figure 1.5: Layout of the ATLAS Inner Detector.

jets, is located at 5 cm from the interaction region. Three additional disks are located at each end-cap, producing typically three pixel position measurements per charged particle track. Each layer or disk is instrumented with modules that form the basic unit of data acquisition, each with 47,232 pixels. All pixel sensors are identical and have a minimum pixel size in $r - \phi \times z$ of $50 \times 400 \mu\text{m}^2$. The intrinsic accuracies in the barrel are $10 \mu\text{m}$ in $r - \phi$ and $115 \mu\text{m}$ along z , or along r in the end-caps. The pixel detector has approximately 80.4 million readout channels, an order of magnitude more readout channels than the rest of ATLAS combined, and it extends to a total length of $z \sim \pm 650 \text{ mm}$ and radius of $r \sim 150 \text{ mm}$, providing good reconstruction efficiency for tracks up to $|\eta| < 2.5$.

The SCT

The SCT consists of four barrel layers and nine end-cap layers surrounding the pixel detector, resulting in at least four hits along every charged particle track. The SCT barrel reaches to $z \sim \pm 750$ mm and $r \sim 515$ mm, while the end-cap covers out to $z \sim \pm 2720$ mm and $r = 560$ mm. There are 15,912 SCT module sensors, each 12.8 cm long and approximately 285 μm thick.

In the barrel region, these modules use small-angle (40 mrad) stereo strips to measure both coordinates, with one set of strips in each layer parallel to the beam direction, measuring the ϕ coordinate directly . In the end-cap region, the detectors have a set of strips running radially and a set of stereo strips at an angle of 40 mrad. The mean pitch of the strips is 80 μm . The intrinsic accuracies per module in the barrel are 17 μm in $r - \phi$ and 580 μm in z (or r in the end-caps). The total number of readout channels in the SCT is approximately 6.3 million. A hit is registered only if the pulse height in a channel exceeds a preset threshold (~ 1 fC). The charge measured in the strip is then recorded into a memory buffer that is only read out and used for tracking if a trigger is received signaling that the event should be considered in more detail.

The TRT

The TRT surrounds the silicon detectors and is comprised of up to 76 layers of longitudinal straw tubes in the barrel, extending to $z \sim \pm 710$ mm and $r \sim 1060$ mm, and 160 radial straw planes in each end-cap cylinders, reaching $z \sim \pm 2710$ mm and $r \sim 1000$ mm.

The TRT sensors are thin drift tubes consisting of cathode metal straws filled with an ionizing gas mixture of xenon, oxygen, and CO₂, with an anode wire running down the center of the straw. The passage of a charged particle

through the gas produces positive ions and free electrons, which travel to the cathode and anode, respectively, under the influence of an applied voltage of 1600 V. Comparing the time that the signals are received at the cathode and the anode gives a drift time measurement that can be used to calculate the impact parameter of the particle. This method gives no information on the position along the length of the straw.

To give the best resolution of particle trajectories as they bend in the solenoidal field, the straws lie along the beam direction in the barrel and radially in the end-caps. The straw diameter of 4 mm causes a maximum drift time of approximately 48 ns and an intrinsic accuracy of 130 μm along the radius of the straw.

In addition to directly detecting charged particles produced by the collision, the TRT also measures the transition radiation induced by the passage of these particles through polypropylene sheets placed between the drift tube straws. Transition radiation refers to the photons emitted by charged particles as they pass from one material into another with a different dielectric constant. These photons yield a much larger signal amplitude than the charged particles, so separate thresholds in the electronics can be used to distinguish the two.

One of the most important tasks of the inner detector is to provide accurate collision vertex identification, exploiting the excellent position resolution and tracking efficiency. Vertices are reconstructed by matching inner detector tracks with $p_T > 150$ MeV back to a common origin.

1.2.2 The Calorimeter System

The purpose of the ATLAS calorimeter system is to measure the energy of electrons, photons, taus and jets, within the pseudorapidity region of $|\eta| < 4.9$

and with full ϕ symmetry and coverage around the beam axis. It also provides fast position and energy measurements to serve as trigger signals for these objects as well as the missing transverse energy.

The calorimeter detector consist of electromagnetic (EM) calorimeter and hadronic calorimeter components. The EM calorimeter provides fine granularity measurements of electrons and photons. Each calorimeter is segmented both transverse to the particle direction, to give position information, and along the particle direction, to chart the development of the particle shower. This permits detailed mapping of EM and hadronic showers in the calorimeter, allowing for studies of the internal structure of hadronic jets and partially giving rise to the high resolution measurements of their energy.

The EM and hadronic calorimeters are sampling calorimeters meaning that they utilize alternating layers of absorber material, composed of heavy atoms that interact with energetic particles and cause them to loose energy, and an active material, that produce a signal in response to the deposited energy.

The calorimeters closest to the beam-line are housed in three cryostats, one barrel and two end-caps. The barrel cryostat contains the electromagnetic barrel calorimeter, and the two end-cap cryostats each contain an electromagnetic end-cap calorimeter (EMEC), a hadronic end-cap calorimeter (HEC), located behind the EMEC, and a forward calorimeter (FCal) to cover the region closest to the beam. These calorimeters use liquid argon as the active detector medium and need to be mantained at a constant temperature of $\sim 88\text{K}$. Liquid argon (LAr) has been chosen for its intrinsic linear behaviour (production of ionization charge as a function of incident charge), its stability of response over time and its intrinsic radiation-hardness.

An illustration of all these components can be found in Fig. 1.6. Further

specifications are given in the next sections.

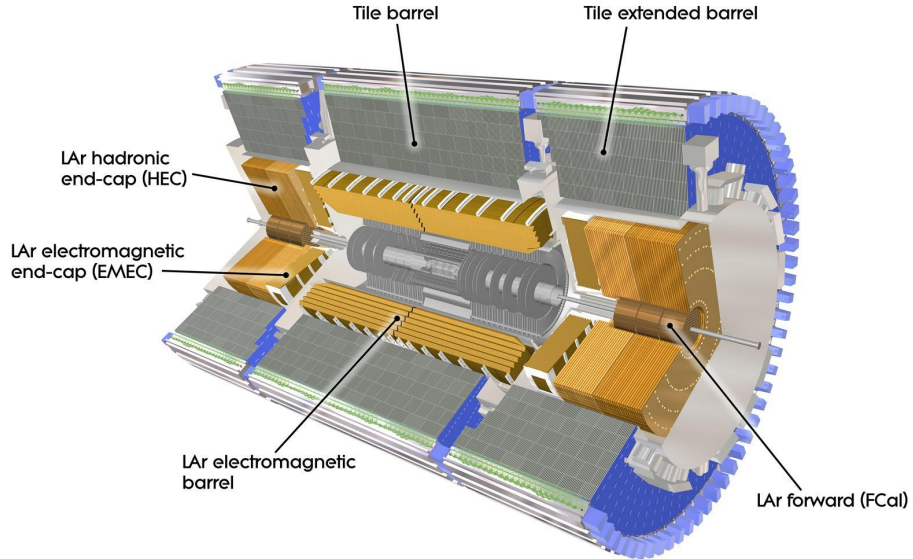


Figure 1.6: Layout of the ATLAS electromagnetic and hadronic calorimeter systems. The total length is ~ 12 m, extending to a maximum radius of 4.25 m.

Liquid argon EM calorimeter

The EM calorimeter uses lead as the absorber and liquid Argon as the active material. A photon traversing the absorber will interact with the heavy nucleus via Compton scattering or the photo-electric effect, producing low-energy electrons, or pair production, producing electron/positron pairs. An electron or positron, in turn, can produce bremsstrahlung photons as it is deflected by the nuclei or produce more charged particles via ionization. Thus each incident photon, electron, or positron produces a shower of photons, electrons, and positrons that lose their energy through successive interactions

in the absorber. The produced particles ionize the liquid argon, and the charge is collected by electrodes located in the liquid argon gap. These electrodes consist of three layers of copper sheets, the outer two kept at high-voltage potential and the inner one used to readout the signal.

To provide full coverage in ϕ without any cracks, an accordion-shaped absorber and electrode geometry is used, shown in Fig. 1.7. This design was chosen to ensure high azimuthal uniformity, a regular liquid argon ionization gap, and a constant sampling fraction within a given detector region. The figure highlights how this geometry is divided among rectangular cells in $\eta \times \phi$ space, the individual readout elements of varying size, finely segmented both laterally and longitudinally. Such fine segmentation $\Delta\eta \times \Delta\phi = 0.025 \times 0.025$ in the second layer of the EM barrel, for example permits a detailed mapping of the electromagnetic and hadronic showers.

The position resolution of the EM is driven by the readout geometry (rectangular cells). There are three layers of cells, segmented along the particle’s direction of motion. The ϕ segmentation comes from grouping the accordion-shaped electrodes together into a common read out channel.

In the region $0 < |\eta| < 1.8$ the electromagnetic calorimeters are complemented by a “presampler” detector, an instrumented argon layer, which provides a measurement of the energy lost in the solenoid and the outer wall of the barrel cryostat.

The EMEC uses the same accordion geometry as the EMB, whereas the granularity is typically slightly larger than in the barrel.

The signal readout chain for the LAr calorimeter (indeed for all calorimeter systems) is divided into a fast analog readout for the trigger system and a slower digital readout used for more redefined trigger decisions and the offline reconstruction. However, regardless of the readout path, the signal

is initiated within the active LAr medium. To minimize noise and increase speed the first level of readout is located on the detector (both for LAr and Tile calorimeter, see 1.2.2). The front-end electronics amplify and shape the signal. Shaping electronics induce a bipolar pulse shape in the ionization signal. This shape is characterized by having both a positive and a negative component, which renders the integral of the signal exactly equal to zero.

The performance of the shaping electronics is critical for a correct energy calibration of the detector since the energy is primarily determined from the peak height of the pulse. In each calorimeter region, the overall pulse shape and duration are optimized to approximately cancel a constant injection of energy into the detector. The motivation for this approach is to effectively redefine the baseline of the energy measurement. In the high luminosity environment of the LHC, this reduces the sensitivity to the background from multiple pp interactions on average.

To translate these analog signals to digital signals that can be transmitted long distances to the next stage of the readout system, the pulse shape is measured over several 25 ns (nominal) time intervals, known as samples. The challenge of calorimeter calibration is to map these measured signals to the energy deposited in the active detector medium, known as the visible energy. This calibration is established using test-beam measurements of electrons in the EMB [8, 9, 10, 11] and EMEC calorimeters [12, 13].

The hadronic calorimeter

Outside the EM calorimeter lies the system of hadronic calorimeters. The barrel portion, known as the Tile calorimeter, uses iron absorber slabs interspersed with scintillating tiles. The Tile calorimeter is most notable for its

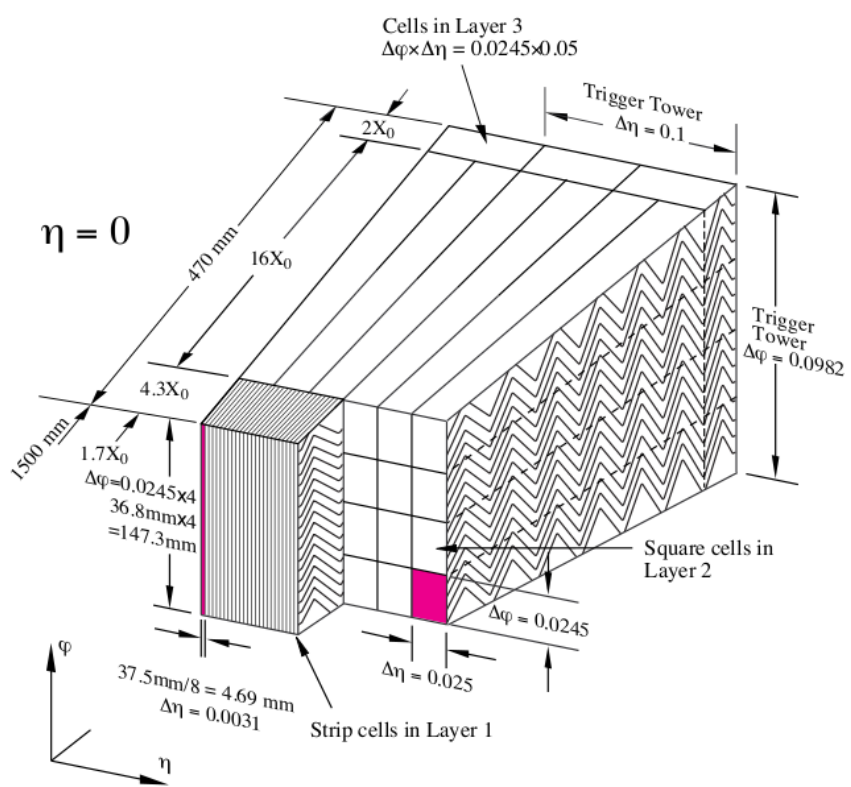


Figure 1.7: Cross section of the LAr barrel calorimeter where the different layers are visible. The granularity in η and ϕ of the cells of each of the three layers is also shown.

depth of 7.4 radiation lengths (λ^1). The hadronic end-cap and the forward calorimeter, which need to absorb the more energetic particles that are produced at large $|\eta|$, are made of copper and tungsten absorbers, respectively, with liquid argon as the active material.

The tile calorimeter is composed of 3 mm thick scintillating tiles, arranged to lie parallel to the incoming particle direction, interleaved with 14 mm thick iron plates. It is divided into the barrel calorimeter, covering $|\eta| < 1.0$, and two extended barrel calorimeters, covering $0.8 < |\eta| < 1.7$. Each tile is read out by two wavelength-shifting fibers, which convert the scintillator signal to visible light. The readout fibers of several tiles are grouped to a single photomultiplier tube forming cells in $\eta \times \phi$ space. As in the EM calorimeter, these cells are segmented into three layers, the first two of size $\Delta\eta = 0.1$ and $\Delta\phi = 0.1$ and the last of size $\Delta\eta = 0.2$ and $\Delta\phi = 0.1$. Towers to provide information to the trigger system are formed from 0.1×0.1 grouping of all three layers.

The HEC uses the LAr active readout design due to the higher radiation tolerance required for the forward regions. Although housed in the same cryostat as the accordion geometry EMEC, the HEC implements a flat-plate design.

The forward calorimeter extends to cover the region $3.1 < |\eta| < 4.9$. Since it is the only calorimeter that covers this very forward region, it must provide both electromagnetic and hadronic measurements. In addition, the high particle fluxes in this region necessitate a finely granulated design. The FCal is approximately 10 interaction lengths deep, and consists of three modules in

¹To quantify the amount of material needed to capture a particle's energy, the unit of an interaction length, which is the distance over which a high energy charged particle loses $1 - \frac{1}{e} \sim 63\%$ of its energy, is commonly used.

each end-cap: the first, made of copper, is optimised for electromagnetic measurements, while the other two, made of tungsten, measure predominantly the energy of hadronic interactions.

The hadronic calorimeters are calibrated using muons in test-beam experiments and those muons produced by cosmic-rays in situ. The invariant mass of the Z boson in $Z \rightarrow ee$ events measured in-situ in the 2010 pp collisions is used to adjust the calibration derived from test-beams and cosmic-muons.

1.2.3 The Muon System

The muon system gives the ATLAS detector its overall shape and imposing nature, as depicted in Fig. 1.8. Muons have much smaller cross section to interact in material than electrons and hadrons, for this, they do not deposit all their energy in the calorimeters. The muon spectrometer is designed to detect muons within $|\eta| < 2.7$. Because many new physics signatures involve high-momentum muons, the system is also required to provide trigger signals based on the particle p_T for $|\eta| < 2.4$.

To provide a momentum measurement, the muons trajectories are bent in a toroidal magnetic field. This field is provided by one large barrel toroid and two large end-cap toroids, each toroid consisting of eight coils arranged symmetrically around the beam axis. The toroid system produces a magnetic field that is typically oriented in the ϕ direction and that is measured with over 1800 Hall sensors placed through the magnets. Under the influence of this field, muons are deflected in the $r-z$ plane and the transverse momentum of the muons is given then by the radius of curvature of the tracks. Since the highly-energetic muons bend very little even in this high magnetic field, the muon system is the largest of all the ATLAS sub-detectors, covering a radius from ~ 4.5 m to ~ 12.5 m.

Four primary subsystems comprise the integrated muon spectrometer: monitored drift tubes (MDT), cathode strip chambers (CSC, which are multiwired proportional chambers with cathodes segmented into strips), resistive plate chambers (RPC) and thin gap chambers (TGC). The MDT and CSC subsystems are primarily designed for precision measurements of muon tracks, with the MDT system providing coverage for the more central region ($|\eta| < 2.7$, with full coverage only in $|\eta| < 2.0$), whereas the CSC is located in the more forward region ($2.0 < |\eta| < 2.7$) due to its ability to cope with higher background rates. The RPC and TGC muon subsystems are designed to provide fast, robust readout for use in the trigger and data acquisition system. A detailed description of the subsystems can be found elsewhere [4].

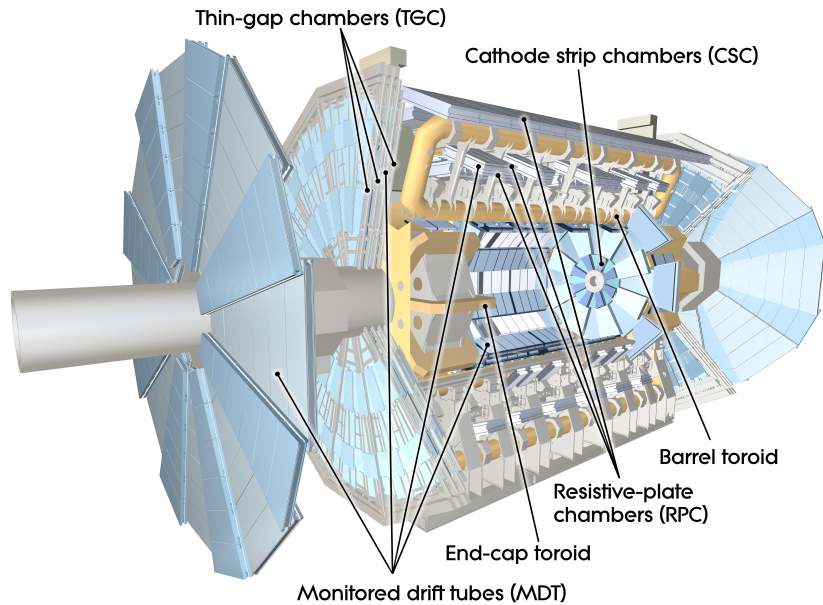


Figure 1.8: The Muon Chamber.

1.2.4 Forward Detectors

Three smaller detector systems cover the ATLAS forward region. The main function of the first two systems is to determine the luminosity delivered to ATLAS. At ± 17 m from the interaction point lies LUCID (LUminosity measurement using Cerenkov Integrating Detector). The principle of LUCID is to detect inelastic $p - p$ scattering in the forward region, exploiting the fact that the number of particles detected is proportional to the total, both primary and pile-up, interactions in a bunch-crossing. LUCID thus provides a relative luminosity measurement, in which the detected number of particles must be translated to the total number of proton-proton interactions via calibration runs. The second detector is ALFA (Absolute Luminosity For ATLAS). Located at ± 240 m, it consists of scintillating fibre trackers located inside Roman pots which are designed to approach as close as 1 mm to the beam. The third system is Zero-Degree Calorimeter (ZDC), which place a role in determining the centrality of heavy-collisions.

1.2.5 Trigger and Data Adquisition System

At design luminoisty, the LHC will deliver approximately 40 million collision events every second. With an average ATLAS event size of ~ 1.5 MB, this is far more information than can be saved into the finite data storage resources available. The goal of the trigger system is to move interesting physics events to permanent storage, while rejecting the vast majority of other events.

The online selection is done in three stages: the Level 1 (L1), Level 2 (L2) and Event Filter (EF) stages. Each trigger level refines the decisions made at the previous level and, where necessary, applies additional selection criteria. The data acquisition (DAQ) system receives and buffers the event data from

the detector-specific readout electronics, at the L1 trigger accept rate, over 1600 point-to-point readout links. The L1 trigger uses a limited amount of the total detector information (only from the calorimeter and the muon systems) using only simple hardware based algorithms to make a decision in less than $2.5\ \mu\text{s}$, reducing the rate to about 75 kHz. The L2 and EF, collectively referred to as the High Level Trigger (HLT), are based on fast software algorithms running on large farms of commercial processors. The L2 is the first stage of the ATLAS DAQ system that has access to data from the ID and is capable of doing partial reconstruction of events up to the L1 accept rate. L2 trigger is designed to reduce the rate to approximately 3.5 kHz, with an event processing time of about 40 ms, averaged over all events. The EF reduces the rate to roughly 200 Hz. Its selections are implemented using offline analysis procedures within an average event processing time of the order of 4 s.

The L1 trigger is designed to accept high- p_T muons, electrons, photons, jets, and taus, as well as events with large missing transverse energy or sum energy. It uses signals from the TGCs and RPCs from muon triggers and reduced granularity calorimeter information for electron, photon, jet, tau and total energy triggers. The calorimeter trigger system, which maintains a fast readout independent from the remainder of the calorimeter is known as the Level-1 Calorimeter. At this level coarse calorimeter information is available in the form of jet elements with $\Delta\eta \times \Delta\phi = 0.2 \times 0.2$ for $|\eta| < 3.2$. Jets are reconstructed using a square sliding window algorithm. In addition to coarse jets, the total transverse energy is also measured at the L1. The region of the detector corresponding to the location where the L1 thresholds were passed – so called “region of interest” (RoI) – are then delivered to the L2 software algorithms.

The L2 trigger applies additional energy thresholds and multiplicity requirements using the RoI around triggered L1 objects. For example, the L2 jet trigger retrieves the data from cells surrounding the L1 RoI and constructs jets using a simplified cone jet algorithm.

The next step and last stage in the trigger chain is the EF, which receives events that have been selected by the L2 triggers and processes the entire event with the full detector granularity instead of only a restricted region.

The monitoring infrastructure of the HLT supports the real-time accumulation of histograms, and their aggregation across the farm, so that parameters can be extracted from cumulative distributions that contain events from all processor nodes. Beam parameters determined from those live histograms are transmitted online to the LHC and are also available to feed back into the HLT itself for use by its own trigger algorithms that depend on the precise knowledge of the luminous region.

1.2.6 ATLAS performance and data quality

The ATLAS detector has been operational for a number of years collecting large amounts of data. Before the start-up of the LHC, measuring muons from cosmic rays; which were used to test, understand, and align the detector. In 2010 and 2011 ATLAS recorded over 5.2fb^{-1} of collision data. Fig. 1.3 presented the luminosity delivered by the LHC in 2011 as well as the recorded luminosity by the detector, showing a good performance of the ATLAS Experiment. The fraction of time that each subdetector system was operational during data-taking is shown in Table 1.2.

The Data Quality (DQ) selection within ATLAS is based on the inspection of a standard set of distributions that lead to a data quality assessment which is encoded in so-called DQ flags. DQ flags are issued for each de-

tector, usually segmented in subdetectors like barrel, end-caps and forward. DQ flags are also issued for trigger slices and for each physics object reconstruction. In this way, the state of the ATLAS detector from hardware to physics object reconstruction is expressed through DQ flags, which are saved per luminosity block. A luminosity block is a time interval of typically two minutes.

The DQ information is used in analyses through dedicated lists of good runs/luminosity blocks. Good run lists are formed by DQ selection criteria in addition to other criteria, such as run range, magnetic field configuration and beam energy. A complete list of valid physics runs and luminosity blocks is used in each analysis.

| Detector component | operational |
|---------------------|-------------|
| Inner Detector | |
| Pixel | ≈96.4% |
| SCT | ≈99.2% |
| TRT | ≈97.5% |
| Calorimeter | |
| EM | ≈99.8% |
| Tile | ≈96.2% |
| Hadronic, end-cap | ≈99.6% |
| Forward calorimeter | ≈99.8% |
| Muon Spectrometer | |
| MDT | ≈99.7% |
| CSC | ≈97.7% |
| RPC | ≈97.0% |
| TGC | ≈97.9% |

Table 1.2: The approximate fraction of time that each individual subdetector system was operational during data-taking.

Chapter 2

Event reconstruction and *b*-Tagging

The event reconstruction packages, which in ATLAS are implemented in the software framework ATHENA [14], process the events, starting from the raw data obtained from the various sub-detectors (energy deposits and hits), through different stages to finally interpreting them as a set of charged tracks, electrons, photons, jets, muons and, in general, of possible kinds of final state objects with related four momenta. In this chapter the reconstruction of these objects is briefly described together with the algorithms for the identification of *b*-quark jets. These algorithms are mainly based on the reconstruction of the primary interaction vertex, on the reconstruction of charged particles in the Inner Detector and on the reconstruction of jets in the calorimeter.

2.1 Jet reconstruction and calibration

Hadronic jets used for ATLAS analyses are reconstructed by a jet algorithm, starting from the energy depositions of electromagnetic and hadronic showers

in the calorimeters. The ATLAS performance group, addressing the calibration of jets and the missing transverse energy (Jet/E_{miss}), has made the decision to adopt the anti- k_t algorithm (Chapter ??) as its default jet algorithm. This choice was driven by multiple requirements ranging from physics performance to those intimately involved with the computing, trigger and detector. The anti- k_t algorithm is fast and its memory consumption is low. It is well adapted to algorithms used in the trigger and has the best jet reconstruction efficiency at low p_T . It exhibits the smallest fluctuations of the jet area (it is the most cone-like) showing good stability under pile-up [15].

Two different size parameters are used: $R = 0.4$, for narrow jets, more adequate to describe the event substructure and associate matrix element partons to jets in multiparton final states; and $R = 0.6$, for wider jets, with very little out of cone radiation, more suitable for QCD studies.

The input to calorimeter jet reconstruction can be calorimeter towers or topological cell clusters. Charged particle tracks reconstructed in the Inner Detectors are also used to define jets. The latter have the further advantage of being insensitive to pile-up and they provide a stable reference for systematic studies. The jet inputs are combined as massless four-momentum objects in order to form the final four-momentum of the jet, which allows for a well-defined jet mass [16]. In the case of track-jets, the track four-momentum is constructed assuming the π meson mass for each track. In Monte Carlo simulation, reference jets (“truth jets”) are formed from simulated stable particles using the same jet algorithm as for the calorimeter jets.

Calorimeter towers are static, $\Delta\eta \times \Delta\phi = 0.1 \times 0.1$, grid elements built directly from calorimeter cells. There are two types of calorimeter towers: with or without noise suppression. The latter are called “noise-suppressed”, and use only the cells with energies above a certain noise threshold. The

noise of a calorimeter cell is measured by recording calorimeter signals in periods where no beam is present in the acelerator. The standard deviation σ around the mean no-beam energy is interpreted as the noise of the cell, and it depends on the sampling layer in which the cell resides and the position in η .

The results presented in this thesis use jets built from noise-suppressed topological clusters, also known as “topo-clusters” [17]. Topological clusters are groups of calorimeter cells that are designed to follow the shower development taking advantage of the fine segmentation of the ATLAS calorimeters. The topological cluster formation starts from a seed cell with $|E_{cell}| > 4\sigma$ above the noise. In a second step, neighbor cells that have an energy at least 2σ above their mean noise are added to the cluster. Finally, all nearest-neighbor cells surrounding the clustered cells are added to the cluster, regardless of the signal-to-noise ratio¹. The position of the cluster is assigned as the energy-weighted centroid of all constituent cells (the weight used is the absolute cell energy).

Jet calibration

The baseline EM energy scale of the calorimeters is the result of the calibration of the electronics signal to the energy deposited in the calorimeter by electromagnetic showers (see Chapter 1). The purpose of the jet energy calibration, or jet energy scale (JES), is to correct the measured EM scale energy to the energy of the stable particles within a jet. The jet energy calibration must account then for the calorimeter non-compensation; the energy lost in inactive regions of the detector, such as the cryostat walls or cabling; energy

¹Noise-supressed towers also make use of the topological clusters algorithm [17] to select cells, i.e. only calorimeter cells that are included in topo-clusters are used.

that escapes the calorimeters, such as that of highly-energetic particles that “punch-through” to the muon system; energy of cells that are not included in clusters, due to inefficiencies in the noise-suppression scheme; and energy of clusters not included in the final reconstructed jet, due to inefficiencies in the jet reconstruction algorithm. The muons and neutrinos that may be present within the jet are not expected to interact within the calorimeters, and are not included in this energy calibration. Due to the varying calorimeter coverage, detector technology, and amount of upstream inactive material, the calibration that must be applied to each jet to bring it to the hadronic scale varies with its η position within the detector.

A number of complex calibration schemes, taking into account these effects, have been developed in ATLAS. The simplest procedure used for 2011 data, referred to as “EM+JES” calibration, utilizes an energy and η -dependent calibration scheme that is primarily based on Monte Carlo simulation with some direct in-situ measurements. This is the calibration used in this thesis. It consists of three subsequent steps:

- Pile-up correction: An offset correction is applied in order to subtract the additional average energy measured in the calorimeter due to multiple proton-proton interactions. This correction is derived from minimum bias data as a function of NPV, the jet pseudorapidity and the bunch spacing. This additional energy is subtracted before the hadronic energy scale is restored such that the derivation of the jet energy scale calibration is factorized and does not depend on the number of interactions in the event.
- Vertex correction: The jet four momentum is corrected such that the jet originates from the primary vertex of the interaction instead of the geometrical centre of the detector.

- Jet energy and direction correction: The jet energy and direction are corrected using constants derived from the comparison of the kinematic observables of reconstructed jets and those from truth jets in the simulation.

In the final step the calibration is derived in terms of the energy response of the jet, or the ratio of the reconstructed jet energy to that of a “truth” jet built of all truth stable interacting particles in the Monte Carlo. This response, written as

$$\mathcal{R} = E_{reco}/E_{truth} \quad (2.1)$$

may be defined at any energy scale. In Equation 2.1, E_{truth} is the energy of the closest isolated truth jet, within $\Delta R < 0.3$. This value was chosen because it results in a reconstructed-to-truth jet match more than 99% of the times. The isolation requirement is applied in order to factorize the effects due to close-by jets from those due to purely detector effects such as dead material and non-compensation. The isolation criterion requires that no other jet with a $p_T > 7$ GeV be within $\Delta R < 2.5R$, where R is the distance parameter of the jet algorithm.

The jet energy response is binned in truth jet energy and the calorimeter jet η . For each (E_{truth}, η) -bin, the averaged jet energy (p_T) response is defined as the peak position of a Gaussian fit to the E_{reco}/E_{truth} (p_T^{reco}/p_T^{truth}) distribution.

The EM+JES calibration constants consist in the inverse of the response: $\mathcal{C}(p_T^{EM}) = \mathcal{R}_{reco}^{-1}(p_T^{EM})$, where \mathcal{C} is the calibration constant, \mathcal{R}_{reco} is the response calculated as a function of reconstructed jet p_T . They are derived as a function of p_T^{truth} , to remove the impact of the underlying p_T spectrum on the response. The response, determined as a function of p_T^{truth} , \mathcal{R}_{truth} , is used to apply the constants as a function of p_T^{EM} , that is $\mathcal{R}_{reco}(p_T^{EM}) =$

$\mathcal{R}_{truth}(\mathcal{R}_{truth} \times p_T^{truth})$. This relationship is valid in ATLAS due to the linearity of the jet response as a function of p_T .

A function $\mathcal{F}_{calib,k}(E_{EM}^{jet})$ is then defined for each η -bin k that describes the response as a function of the uncalibrated jet energy. $\mathcal{F}_{calib,k}(E_{EM}^{jet})$ is parameterised as:

$$\mathcal{F}_{calib,k}(E_{EM}^{jet}) = \sum_{i=0}^{N_{max}} a_{i,k} (\ln E_{EM}^{jet})^i, \quad (2.2)$$

where a_i are free parameters, and N_{max} is chosen between 1 and 6 depending on the goodness of the fit. The final jet energy scale correction that relates the measured calorimeter jet energy scale to the hadronic scale is then defined as $1/\mathcal{F}_{calib,k}(E_{EM}^{jet})$ in the following:

$$E_{EM+JES}^{jet} = \frac{E_{EM}^{jet}}{\mathcal{F}_{calib}(E_{EM}^{jet})|_\eta}, \quad (2.3)$$

where $\mathcal{F}_{calib}(E_{EM}^{jet})|_\eta$ is $\mathcal{F}_{calib,k}(E_{EM}^{jet})$ for the relevant η -bin k .

Other calibrations schemes are the global calorimeter cell weighting (GCW) calibration and the local cluster weighting (LCW) calibration. The GCW scheme exploits the observation that electromagnetic showers in the calorimeter leave more compact energy depositions than hadronic showers with the same energy. Energy corrections are derived for each cell within a jet. The cell corrections account for all energy losses of a jet in the detector. Since these corrections are only applicable to jets and not to energy depositions, they are called “global” corrections.

The LCW calibration method first classifies topo-clusters as either electromagnetic or hadronic, based on the measured energy density. Energy corrections are derived according to this classification from single charged and neutral pion Monte Carlo simulations. Dedicated corrections are derived for the effects of non-compensation, signal losses due to noise threshold

effects, and energy lost in non-instrumented regions. Since the energy corrections are applied without reference to a jet definition they are called “local” corrections. Jets are then built from these calibrated clusters using a jet algorithm.

The final jet energy calibration can be applied to EM scale jets, with the resulting calibrated jets referred to as EM+JES, or to LCW (GCW) calibrated jets, with the resulting jets referred to as LCW+JES (GCW+JES) jets.

A further jet calibration scheme called global sequential (GS) calibration, starts from jets calibrated with the EM+JES calibration and corrects the energy jet-by-jet, without changing the average response. This scheme exploits the topology of the energy deposits in the calorimeter to characterise fluctuations in the jet particle content of the hadronic shower development. Correcting for such fluctuations can improve the jet energy resolution. The correction uses several jet properties, and each correction is applied sequentially.

For the 2011 data the recommended calibration schemes were the EM+JES and the LCW calibrations. The simple EM+JES calibration does not provide the best resolution performance, but allows in the central detector region the most direct evaluation of the systematic uncertainties from the calorimeter response to single isolated hadrons measured *in situ* and in test-beams and from systematic variations in the Monte Carlo simulation. For the LCW+JES calibration scheme the JES uncertainty is determined from *in situ* techniques. For all calibration schemes, the JES uncertainty in the forward regions is derived from the uncertainty in the central region using the transverse momentum balance in events where only two jets are produced.

Jet energy scale uncertainties for the EM+JES scheme

For many physics analyses, the uncertainty on the JES constitutes the dominant systematic uncertainty because of its tendency to shift jets in and out of analysis selections due to the steeply falling jet p_T spectrum. The uncertainty on the EM+JES scale is determined primarily by six factors: varying the physics models for hadronization and parameters of the Monte Carlo generators, evaluating the baseline calorimeter response to single particles, comparing multiple models for the detector simulation of hadronic showers, assessing the calibration scales as a function of pseudorapidity, and by adjusting the JES calibration methods itself. The final JES uncertainty in the central region, $|\eta| < 0.8$, is determined from the maximum deviation in response observed with respect to the response in the nominal sample. For the more forward region, the so called “ η -intercalibration” contribution is estimated. This is a procedure that uses direct di-jet balance measurements in two-jet events to measure the relative energy scale of jets in the more forward regions compared to jets in a reference region. The technique exploits the fact that these jets are expected to have equal p_T due to transverse momentum conservation. Figure 2.1 shows the final fractional jet energy scale uncertainty and its individual contributions as a function of p_T for a central η region. The JES uncertainty for anti- k_t jets with $R = 0.4$ is between $\approx 4\%$ (8%, 14%) at low jet p_T and $\approx 2.5\%-3\%$ (2.5%-3.5%, 5%) for jets with $p_T > 60$ GeV in the central (endcap, forward) region.

In addition to the tests above, *in situ* tests of the JES using direct γ -jet balance, multi-jet balance, and track-jets indicate that the uncertainties in Fig. 2.1 reflect accurately the true uncertainties in the JES.

In the case of jets induced by bottom quarks (b -jets), the calorimeter response uncertainties are also evaluated using single hadron response mea-

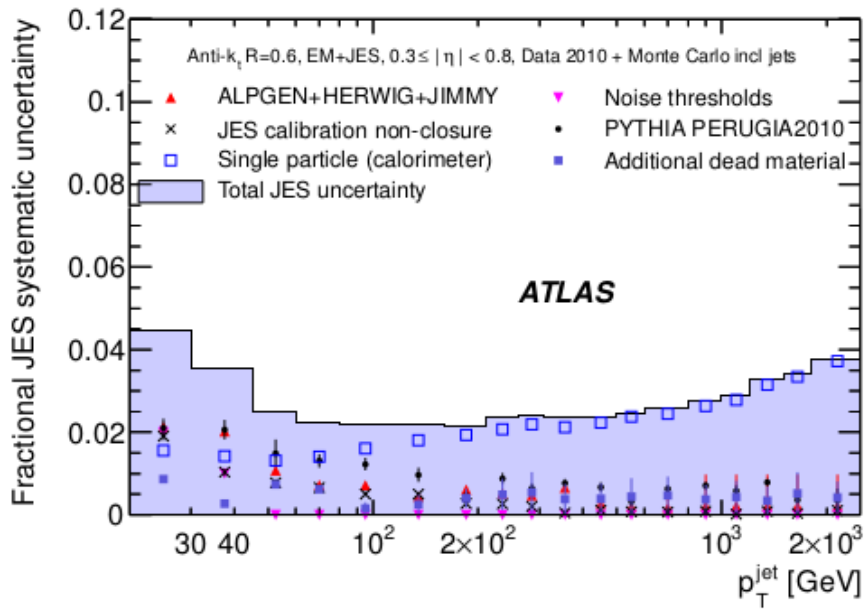


Figure 2.1: Fractional jet energy scale uncertainty as a function of jet p_T for jets in the pseudorapidity region $0.3 < |\eta| < 0.8$ in the calorimeter barrel. The total uncertainty is shown as the solid tight blue area. The individual sources are also shown.

surements *in situ* and in test beams [18]. For jets within $|\eta| < 0.8$ and $20 \leq p_T < 250$ GeV the expected difference in the calorimeter response uncertainty of identified b -jets with respect to the one of inclusive jets is less than 0.5%. It is assumed that this uncertainty extends up to $|\eta| < 2.5$.

The JES uncertainty arising from the modelling of the b -quark fragmentation can be determined from systematics variations of the Monte Carlo simulation. The fragmentation function is used to estimate the momentum carried by the b -hadron with respect to that of the b -quark after quark fragmentation. The fragmentation function included in PYTHIA originates from a detailed study of the b -quark fragmentation function in comparison with OPAL [19] and SLD [20] data. To assess the impact of the b -fragmentation, the nominal parameters of the PYTHIA fragmentation function are replaced by the values from a tune using the Professor framework [21]. In addition, the nominal fragmentation function is replaced by the modified Bowler-Lund fragmentation function [22]. The b -jet response uncertainty is evaluated from the ratio between the response of b -jets in the varied Monte Carlo samples to the nominal PYTHIA. The response variations are well within 2%.

The b -jet JES uncertainty is obtained adding the calorimeter response uncertainty and the uncertainties from the systematic Monte Carlo variations in quadrature. The resulting additional JES uncertainty for b -jets is shown in Fig. 2.2. It is about 2% up to $p_T \approx 100$ GeV and below 1% for higher p_T . To obtain the overall b -jet uncertainty this uncertainty is added in quadrature to the JES uncertainty for inclusive jets.

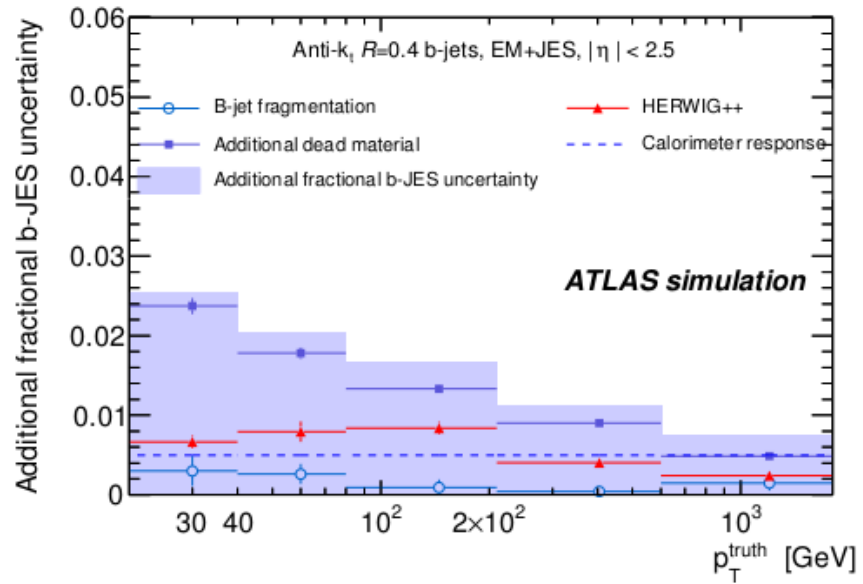


Figure 2.2: Additional fractional b -jet JES uncertainty as a function of the truth jet transverse momentum for anti- k_t jets with $R = 0.4$ calibrated with the EM+JES scheme for $|\eta| < 2.5$. Shown are systematic Monte Carlo variations using different modelling of the b -quark fragmentation and physics effects as well as variations in the detector geometry and the uncertainty in the calorimeter response to b -jets as evaluated from single hadron response measurements. Uncertainties in the individual points are statistical only.

2.2 Reconstruction of charged particle tracks

The Inner Detector layout and the characteristics of its main sub-detectors were presented in Section 1.2.1 of Chapter 1. The tracking algorithm is based on a modular software framework, which is described in more detail in Ref. [23]. The main steps of the tracking algorithm are the following:

- Firstly, the raw data from the pixel and SCT detectors are converted into clusters, while the TRT raw timing information is turned into calibrated drift circles. The SCT clusters need to be further transformed into space-points, by combining the clusters information from opposite sides of the SCT module (stereo strip layers).
- In a second stage, the track-finding is performed, in which the pattern recognition and a global χ^2 minimization procedure is implemented as a default.

In the track-finding stage, track seeds are found in the first three pixel layers and in the first SCT layer. These are extended throughout the SCT to form track candidates and a first track fit is performed. Afterwards, ambiguities in the track candidates found in the silicon detectors are resolved, and tracks are extended into the TRT (which covers up to $|\eta| < 2.$, while Pixel and SCT cover up to 2.5). The final track candidate is refitted with the full information from the three tracking subdetectors. The baseline algorithm is designed for the efficient reconstruction of primary charged particles. Primary particles are defined as particles with a meanlife of greater than 3×10^{-11} s directly produced in a proton-proton interaction, or from the subsequent decays or interactions of particles with lifetime shorter than 3×10^{-11} s. The tracks reconstructed in this stage are required to have $p_T > 400$ MeV.

In a complementary stage, a track search starts from segments reconstructed in the TRT and extends them inwards by adding silicon hits, which is referred to as “back-tracking”. This recovers tracks for which the first hits in the pixel layers are missing, e.g. because they originate from secondaries, which are produced in decays or the interaction of primaries.

The final reconstructed track trajectory is usually specified at its closest point to the interaction region on the transverse plane by its impact parameters in the transverse plane and in the longitudinal direction, respectively called d_0 and z_0 ², and by its momentum, typically expressed in azimuthal angle ϕ , polar angle θ and inverse momentum $1/p$.

The track reconstruction efficiency is defined as the fraction of primary particles with $p_T > 400$ MeV and $|\eta| < 2.5$ matched to a reconstructed track. The reconstruction efficiency for primary tracks with transverse momentum above 1 GeV and central η is above 80%, going down to values below 70% for tracks at the edge of the Inner Detector acceptance [5]. The dense environment of a jet decreases the track reconstruction efficiency and increases the fake rate. This is caused by the occurrence of shared hits between different tracks, which makes the pattern recognition and track fitting tasks more difficult.

The relative transverse momentum scale and resolution of tracks is defined as the Gaussian mean and width of

$$p_T^{MC} \times (1/p_T^{MC} - 1/p_T^{reco}) = 1 - \frac{p_T^{MC}}{p_T^{reco}} \quad (2.4)$$

where p_T^{MC} (p_T^{reco}), refers to the track’s transverse momentum given by simulation truth (MC) or by reconstruction (reco). It should be noted that

²Strickly speaking the impact parameter is $|z_0| \sin \theta$, where θ is the polar angle of the track.

the $(1/p_T)$ resolution is used instead of $\sigma(p_T)$ as the Inner Detector measures the sagitta and not directly the transverse momentum³. However, the resolution obtained from the equation above is the relative transverse momentum resolution, $\sigma(p_T)/p_T$. At low p_T the multiple scattering dominates the resolution, and at high momenta, the resolution is limited by the bending power of the solenoid field and by the intrinsic detector resolution. For a central track with $p_T = 5$ GeV the transverse momentum resolution is around 75 MeV and the transverse impact parameter resolution is about 35 μm .

2.3 Vertex reconstruction

Primary vertices are reconstructed using an iterative vertex finding algorithm [24]. In a first step, a dedicated vertex finding algorithm associates tracks to vertex candidates. Vertex seeds are obtained by looking for the global maximum in the distribution of the z coordinates of the tracks. In a second stage, an iterative χ^2 fit is made using the seed and nearby tracks. Each track carries a weight which is a measure of its compatibility with the fitted vertex depending on the χ^2 of the fit. Tracks displaced by more than 7σ from the vertex are used to seed a new vertex and the procedure is repeated until no additional vertices can be found. The parameters of the beam spot are used both during the finding to preselect compatible tracks and during the fitting step to constrain the vertex fit.

The knowledge of the position of the primary interaction point (primary vertex) of the proton-proton collision is important for b -quark jets identification since it defines the reference point with respect to which impact parameters and vertex displacements are measured. The typical vertexing

³The relation between sagitta s and transverse momentum (p_T) is given by $s \sim 1/p_T$.

resolution in z is $\mathcal{O}(100\mu\text{m})$.

To ensure a good resolution on the vertex position, the primary vertex must be reconstructed from at least five tracks. The choice of the primary vertex is less trivial in the presence of minimum-bias events from pile-up: the primary vertex from a pile-up event may be mistakenly used as the signal vertex, or a fake primary vertex built from tracks from two different vertices may be reconstructed. The current strategy is to choose the primary vertex candidate that maximizes $\sum_{\text{tracks}} p_T^2$.

2.4 b -jet Tagging

The ability to identify jets originating from *bottom*-quarks (denoted as b -tagging in the following) is important for the high- p_T physics program of a general-purpose experiment at the LHC such as ATLAS since many interesting physics processes contain b -quarks in the final state, while the most abundant backgrounds contain mostly up, down and strange quark or gluon jets or, in a smaller fraction of cases, charm quark jets. The aim of b -tagging is therefore to identify the b -quark jets with high efficiency, while rejecting most of the background contamination from jets originating from the fragmentation of light (u , d , and s) quarks, gluons and c -quarks.

A b -quark, once produced, fragments necessarily into a b -flavoured hadron, b -hadron in the following. In most of the cases ($\approx 87\%$), first an excited b -hadron is produced, like a B^* or a B^{**} , which decays immediately, strongly or electromagnetically, into a ground state b -hadron plus one or more further particles; while in the remaining cases, a ground state b -hadron is produced directly. One is only interested in the transition from a b -quark into the final state b -hadron, since the typical timescale for electromagnetic or strong

interactions is so small that the B^* , B^{**} decay vertices are not significantly displaced with respect to the primary vertex. In most of the cases ($\approx 91\%$) a b -meson is produced out of the fragmentation of an original b -quark (40% B^+ , 40% B^0 and 11% B_s^0). The rest are b -baryons.

Due to the b -quark fragmentation function being very hard, most of the original b -quark energy is transmitted to the final b -hadron. This fraction is for example 70% for b -quarks with a momentum of ≈ 45 GeV. This property can be exploited during b -tagging, since the fragmentation for light quarks into light hadrons or c -quarks into c -hadrons is softer.

Any of the finally produced b -hadrons decay through weak interactions and therefore have a significant lifetime, which is on average, for all b -hadrons considered, $(1.568 \pm 0.009) \times 10^{-12}$ s. The effective distance travelled in the detector by the b -hadron before decaying depends on the b -hadron momentum, which enters the relativistic boost factor $\beta\gamma$. A b -quark with momentum of 50 GeV will travel around 3 mm, which is a visible flight length in the detector. Due to the combination of the b -hadron lifetime and relatively high mass ($m_B \approx 5.28$ GeV), which results in a non-negligible decay angle of the b -hadron decay products with respect to the b -hadron flight direction, the charged particles produced at the decay vertex will be on average significantly displaced with respect to the primary vertex position.

This is the main signature which is exploited by the *lifetime* based b -tagging algorithms, which depend either on the presence of significantly displaced tracks, as in impact parameter based b -tagging algorithms, or on the explicit reconstruction of the b -hadron decay vertex, as in secondary vertex based b -tagging algorithms.

b -hadrons decay preferably into a c -hadron plus additional particles⁴. The

⁴Weak decays are governed by the CKM matrix mechanism, and $|V_{cb}|^2 \gg |V_{ub}|^2$.

lifetime of a c -hadron is not much lower than for b -hadrons, but in general the momentum of the c -hadron will be lower than the original b -hadron momentum. However, the c -hadron can still travel for a significant path in the detector and form with its decay products a visible *tertiary* vertex.

Another property which is usually exploited by b -tagging is the fraction of b - and c -hadron decays into leptons: a lepton from the semi-leptonic decay of a b -hadron ($b \rightarrow l$) or from the subsequent c -hadron decay ($b \rightarrow c \rightarrow l$) is produced in $\approx 21\%$ of the cases. This is valid both in case the lepton is an electron or a muon, which brings the overall fraction of b -quarks ending up into final state containing a lepton to $\approx 42\%$. Due to the b - or c -hadron mass, the lepton will be emitted with an average transverse momentum comparable with m_{b-had} or m_{c-had} . By identifying either an electron or a muon originating from a jet and by requiring it to have sufficiently high p_T with respect to the jet axis, it is possible to identify b -jets.

Association of tracks to jets

The b -tagging performance relies critically on the accurate reconstruction of the charged tracks in the ATLAS Inner Detector. The actual tagging is performed on the sub-set of tracks in the event that are associated to jets. The b -tagging algorithm takes as input the three-momenta of the jets, reconstructed by a jet algorithm, and uses the jet direction to associate the charged particles tracks to the jet. Since the 2 Tesla solenoidal magnetic field of the ATLAS Inner Detector bends charged particles in the transverse plane, in particular in the case of low p_T tracks, the tracks are best matched to the jet by using the direction of their momenta at the point of closest approach to the interaction region. The criterion for associating charged particle tracks

to jets is simply:

$$\Delta R(jet, track) < \Delta R_{cut} \quad (2.5)$$

where usually the value of $\Delta R_{cut} = R$ is used; with R , the distance parameter of the jet algorithm used for jet reconstruction.

After the tracks are associated to the jets, they are filtered in order to remove tracks with bad quality or which can easily be erroneously identified as secondary tracks from b -decays. These include tracks originating from decays of even longer lived particles, like K_s^0 ($c\tau \approx 2.69$ cm) and Λ baryons ($c\tau \approx 7.89$ cm); from electromagnetic interactions in the detector material, like conversions in electron-positron pairs ($\gamma \rightarrow e^+e^-$); or from hadronic interactions with the detector material, which result in two or more tracks with high impact parameter. In order to reject badly reconstructed tracks, quality cuts are applied. Requirements are imposed on the number of silicon hits, the track fit quality, the track momentum, and the transverse and longitudinal impact parameters. The track selection needs to be particularly tight in the case of the impact parameter based b -tagging algorithms, since in that case the explicit presence of a vertex is not required, so that the influence of badly reconstructed tracks or tracks from long lived particles does directly limit the performance. The minimum track p_T required is of 1 GeV in the case of the impact parameter based algorithms and of 400-500 MeV otherwise. The transverse and longitudinal impact parameters must fulfill $|d_0| < 1$ mm (3.5 mm) and $|z_0| \sin \theta < 1.5$ mm (no cut on z_0) in the case of the algorithms relying on the impact parameters of tracks (on the reconstruction of secondary vertices). The minimum number of precision hits required is typically 7, for both approaches.

2.4.1 *b*-tagging algorithms

For the 2011 data-taking a set of lifetime taggers were commissioned and calibrated. In this section a brief description of the main features of these algorithms will be given.

Impact parameter based *b*-tagging algorithms

The charged particle tracks originating from *b*-hadrons are expected to have significantly higher transverse and longitudinal impact parameters compared to prompt tracks originating directly from fragmentation. If the effect of long lived particles, conversions and hadronic interactions can be reduced, the best discrimination between prompt tracks and displaced tracks from *b*- and *c*-hadron decays can be obtained using the impact parameter significance, both in the transverse and longitudinal plane, with

$$IP_{r\phi} = d_0 \text{ and } IP_z = z_0 \sin \theta, \quad (2.6)$$

the transverse and longitudinal impact parameter significances are obtained by dividing $IP_{r\phi}$ and IP_z by their respective errors,

$$IP_{r\phi}/\sigma(IP_{r\phi}) \text{ and } IP_z/\sigma(IP_z). \quad (2.7)$$

On the basis that the decay point of the *b*-hadron must lie along its flight path, and in order to increase the discriminating power of the impact parameter significance, a lifetime sign is assigned to these variables (replacing the sign of the geometrical definition of the impact parameter). The sign is positive if the track extrapolation crosses the jet direction in front of the primary vertex (i.e. is more compatible with having its origin in a secondary decay vertex in the direction of flight expected for the *b*-hadron) or negative if the track is more likely to intersect the flight axis behind the primary vertex, opposite to the jet direction. Both cases are illustrated in Fig. 2.3.

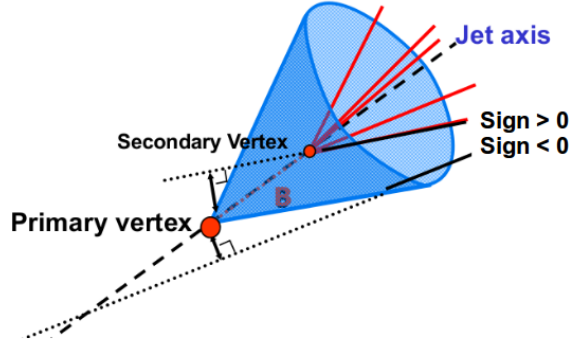


Figure 2.3: Lifetime sign of tracks. A positive and a negative lifetime signed track is shown.

The lifetime sign can be defined in three-dimensions, according to the variables $\vec{p}_{T,jet}$, $\vec{p}_{T,trk}$ and $\vec{\Delta r}_{IP} = \vec{r}_{IP} - \vec{r}_{PV}$, the three-dimensional impact parameter of the track with respect to the primary vertex:

$$\text{sign}_{3D} = \text{sign}([\vec{p}_{trk} \times \vec{p}_{jet}] \cdot [\vec{p}_{trk} \times \vec{\Delta r}_{IP}]). \quad (2.8)$$

The computation of the lifetime sign assumes that the jet direction reproduces, up to a good approximation, the b -hadron direction. Under this assumption and up to resolution effects both on the jet direction and on the impact parameter and momentum of the track, the lifetime sign of tracks originating from b -hadron decays is positive.

The lifetime sign can also be defined on the transverse plane ($x - y$) or on the longitudinal plane ($r\phi - z$) by considering respectively the transverse and longitudinal impact parameters (the projections of the three-dimensional impact parameter on the respective planes):

$$\text{sign}_{r\phi} = \text{sign}(\sin(\phi_{jet} - \phi_{trk}) \cdot d_{0,trk}); \text{ and } \text{sign}_z = \text{sign}((\eta_{jet} - \eta_{trk}) \cdot z_{0,trk}). \quad (2.9)$$

Tracks from the fragmentation in light-jets tend to have a signed impact parameter distribution which is symmetric around 0, since they have no correlation with the jet direction. Tracks from b - and c -hadron decays, as expected, have an asymmetric distribution, with the most significant contribution at positive significances; however a negative tail extending beyond the pure fragmentation contribution is also seen, corresponding to resolution effects and to an eventual mismatch between the b -jet and the b -hadron directions.

The significance, which gives more weight to tracks measured precisely, is the main ingredient of the tagging algorithms based on impact parameters. Now, the impact parameter significance of all N tracks associated to the jet to tag need to be combined into a single discriminating variable. It is assumed that tracks are uncorrelated, so their probability density functions (PDF), defined based on the transverse and/or longitudinal impact parameter significance distributions for the different hypothesis, are uniquely defined as a function of the jet flavour. Using a likelihood function defined according to the product of these PDFs, under the hypothesis of uncorrelated tracks, the following likelihood ratio provides the optimal separation, according to Neyman-Person lemma [25]:

$$\text{LR}(IP_1, IP_2, \dots, IP_N) = \frac{\prod_{i=1}^N \text{PDF}_b(IP_i)}{\prod_{i=1}^N \text{PDF}_l(IP_i)} \quad (2.10)$$

For convention, the discriminant variable used for b -tagging is then defined as:

$$\text{weight}(IP_1, IP_2, \dots, IP_N) = \log(\text{LR}(IP_1, IP_2, \dots, IP_N)) \quad (2.11)$$

Using such a formalism, two impact parameter based b -tagging algorithms are constructed, based on the definition of $\text{PDF}(IP_i)$:

1. IP2D: $\text{PDF}(IP_i) = \text{PDF}(IP_{i,r\phi})$

2. IP3D: $\text{PDF}(IP_i) = \text{PDF}(IP_{i,r\phi}, IP_{i,z})$

In the first case the track PDF is one-dimensional, based on the transverse impact parameter significance. In the second case the PDF is based on a two-dimensional histogram of the transverse and longitudinal impact parameter significance.

The **IP3D** is one of the high-performance tagging algorithms supported for the 2011 data-taking, in which input variables are compared to pre-defined smooth Monte Carlo PDFs for both b -jet and light jet hypotheses [26]. Prior to the use of these advanced tagger, a simpler tagging algorithm, the **Jet-Prob**, combining the impact parameter significances of all tracks associated to the jet was devised to be used for early data, being extensively used during 2010 [27].

The impact parameter based algorithm permits to obtain a very good b -tagging performance, as will be shown at the end of this chapter. This performance can be improved by using some information from the secondary vertex based algorithms in two aspects: tracks associated to long lived particle vertices can be removed from the tracks considered for the impact parameter based algorithms; and, the direction between the secondary and the primary vertex positions can be used to improve the reliability of the lifetime sign, substituting \vec{p}_{jet} with $\vec{r}_{SV} - \vec{r}_{PV}$. The latter improves significantly the estimation of the b -hadron direction. Both kinds of information improve the performance of the impact parameter based b -tagging algorithms.

Secondary vertex based b -tagging algorithms

The typical topology of particle decays in a b -jet is a decay chain with two vertices, one stemming from the b -hadron decay and at least one from c -hadron decays. The reconstruction of these secondary vertices is done in an

inclusive way, where the number of charged particle tracks originating from the b - and c -hadron decays is not known a-priori. An exclusive reconstruction of the huge number of different possible b -decay modes cannot be performed, the set of selection cuts needed to reconstruct all of them would severely limit the reconstruction efficiency.

Two strategies to detect a secondary decay vertex in b -jets are available in ATLAS. The first one is based on the fit of a single geometrical vertex. Even if this hypothesis is not correct, this approximation works well for a large fraction of cases. The second algorithm is based on a kinematic approach, which assumes that the primary event vertex and the b - and the c -hadron decay vertices lie approximately on the same line, the flight path of the b -hadron.

The inclusive fit of a single displaced vertex in b -jets is based on the VKalVrt [28] reconstruction package. The main idea of the algorithm is to maximise the b/c -hadron vertex detection efficiency, keeping at the same time the probability to find a vertex inside a light jet low.

The algorithm begins with all tracks associated to the jet and passing a loose cut selection. The vertex search starts with looking for all track pairs and trying to form a two-track vertex. Each track of the pair must have a three-dimensional impact parameter significance with respect to the primary vertex larger than 2σ and the sum of these two significances must be larger than 6σ . To reduce the influence of badly measured tracks, the two-tracks vertices are required to be produced in the direction of flight of the b -quark, by requiring the scalar product of $(\vec{r}_{2-track} - \vec{r}_{PV}) \cdot \vec{p}_{jet}$ to be positive. Charged particles coming from long lived particles and conversions are not considered. All the tracks corresponding to the accepted two-track vertices are used to determine a single secondary vertex. If the resulting vertex has a very small

vertex probability, the track with the highest contribution to the vertex χ^2 is removed and the vertex fit is repeated until the χ^2 of the fit is good. The result of this procedure is the (eventual) presence of a vertex, its position, and the list of associated tracks.

The **SV1** secondary vertex algorithm uses this procedure to reconstruct inclusive secondary vertices. This advanced tagger takes advantage of three of the reconstructed vertex properties: the invariant mass of all tracks associated to the vertex, the ratio of the sum of the energies of the tracks in the vertex to the sum of the energies of all tracks in the jet, and the number of two-track vertices. These variables are combined using a likelihood ratio technique. SV1 relies on a two-dimensional distribution of the two first variables and a one-dimensional distribution of the number of two-track vertices. In addition the distance ΔR between the jet axis and the line joining the primary vertex to the secondary one is used.

The three-dimensional decay length significance alone, signed with respect to the jet direction can be used as a discriminating variable between b -jets and light jets: this is the principle of the early data **SV0** tagger, extensively used as well with the 2010 and 2011 data [29].

As opposed to the algorithm described above, in which the displaced tracks are selected and an inclusive single vertex is obtained, a second algorithm, called **JetFitter**, is based on a different hypothesis. It assumes that the b - and the c -hadron decay vertices lie on the same line defined through the b -hadron flight path. All charged particle tracks stemming from either decay intersect this b -hadron flight axis. This method has the advantage of reconstructing incomplete topologies, with, for instance, a single track from the b -hadron and a single track from the c -hadron decay. The fit in this case evaluates the compatibility of the given set of tracks with a b - c -hadron

like cascade topology, increasing the discrimination power against light quark jets. The transversal displacement of the c -hadron decay vertex with respect to the b -hadron flight path is small enough not to violate significantly the basic assumption within the typical resolutions of the tracking detector. The discrimination between b -, c - and light jets is based on a likelihood using similar variables as in the SV1 tagging algorithm above, and additional variables such as the flight length significances of the vertices.

Algorithm combinations and performance

The IP3D and SV1 tagging algorithms both use the likelihood ratio method, and due to this they can be easily combined: the weights of the individual tagging algorithms are simply summed up.

The combination of the JetFitter and the IP3D algorithms can be performed using an artificial neural network technique with Monte Carlo simulated training samples and additional variables describing the topology of the decay chain.

Figure 2.4 compares the performance for the various ATLAS b -tagging algorithms described in a simulated sample of $t\bar{t}$ events. It can be seen that by combining the vertexing techniques and the impact parameter information, the IP3D+SV1 and IP3D+JetFitter algorithms can reach very high tagging efficiencies.

The performance of a b -tagging algorithm is usually measured in terms of the *light-jet rejection* obtained for a given *b -jet tagging efficiency*. Curves are obtained by varying continuously the *operating point* of each tagger, i.e. the cut on its output discriminating variable (weight). The b -jet tagging efficiency, ϵ_b , is the fraction of jets labeled as b -jets that are properly tagged while the light-jet rejection, defined as $1/\epsilon_{light}$, is the reciprocal of the fraction

of jets that are labeled as light jets and are actually incorrectly tagged by the algorithm.

The labeling procedure used for b -tagging is based on the flavor of true quarks: a jet is labeled as a b -quark jet if a b -quark is found in a cone of size $\Delta R = 0.3$ around the jet direction. The various labeling hypotheses are tried in this order: b quark, c quark and τ lepton. When none of these hypotheses are satisfied, the jet is labeled as a light jet. No attempt is made to distinguish light jets originating from gluons from those originating from quarks at this stage.

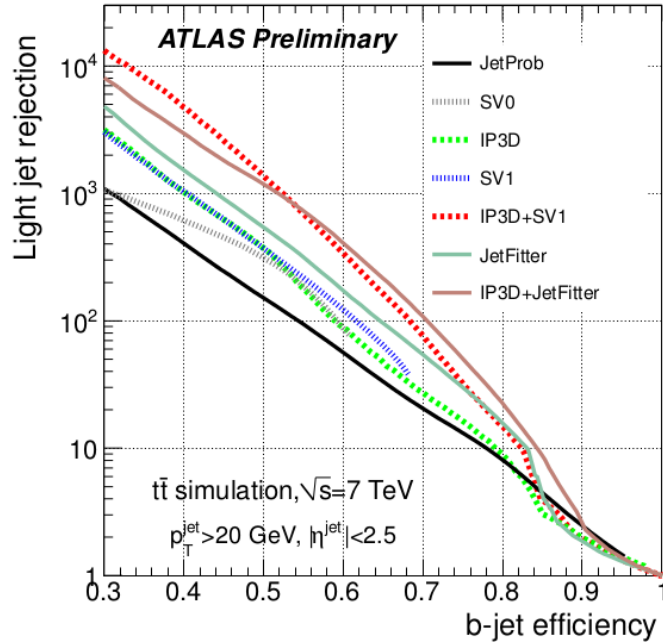


Figure 2.4: Light-jet rejection as a function of the b -jet tagging efficiency for the early tagging algorithms (JetProb and SV0) and for the high-performance algorithms, based on simulated $t\bar{t}$ events.

The MV1 tagging algorithm

The **MV1** b -tagging algorithm is a combined algorithm based on a neural network using the output weights of the IP3D and SV1 algorithms and the JetFitter+IP3D combination as input. Being the best performing algorithm (better light rejection for a given signal efficiency) it is the recommended tagger for 2011 and 2012 analyses. This is the b -tagging algorithm used in this thesis.

2.4.2 b -tagging calibration

In order for b -tagging to be used in physics analyses, the efficiency with which a jet originating from a b -quark is tagged needs to be measured in data. Moreover, an appropriate description of the b -tagging efficiencies based on measurements with data is essential for correctly modelling the measurements in Monte Carlo simulation . A second necessary piece of information is the probability of mistakenly tagging a jet originating from a light-flavour (u -, d -, s -quark or gluon) jet as a b -jet, referred to as the mistag rate. The b -tagging “calibration” includes both the measurement of the mis-tag rates and b -tagging efficiency.

The measurements of the b -tag efficiency and mistag rate are provided in the form of jet p_T - and η -dependent scale factors that correct the b -tagging performance in simulation to that observed in data. The scale factors are defined as the ratio of the b -tag efficiency or mistag rate in data and simulation:

$$\kappa_{\epsilon_b}^{data/sim} = \frac{\epsilon_b^{data}}{\epsilon_b^{sim}}, \quad \kappa_{\epsilon_l}^{data/sim} = \frac{\epsilon_l^{data}}{\epsilon_l^{sim}}, \quad (2.12)$$

where ϵ_b^{sim} and ϵ_l^{sim} are the fractions of b - and light-flavour jets which are tagged in simulated events, with the jet flavour defined by matching to generator level partons as defined in the previous section.

In physics analyses, these p_T -dependent scale factors are then applied as weights to the jets in Monte Carlo simulation, to reproduce the b -tagging performance in data.

The main b -tagging efficiency calibration methods, the so called *system8* and $p_{T\text{rel}}$ methods, are described in detail in ref [30]. These measurements are based on a sample of jets with muons inside, where the muons are serving as a reference b -tagging algorithm to obtain a b -jet sample on which the calibrations can be performed. At the LHC, the large $t\bar{t}$ production cross section of $\sigma_{t\bar{t}} = 177 \pm 3(\text{stat.})^{+8}_{-7}(\text{syst.}) \pm 7(\text{lum.}) \text{ pb}$ [31] offers an alternative source of events enriched in b -jets. Calibrations using samples of $t\bar{t}$ events have been obtained for SV0, IP3D+SV1, JetFitter and MV1 b -tagging algorithms [32]. All these algorithms provide an output weight w , discriminating between b -jets and non- b -jets. Lower values of w are assigned to c - and light-flavour jets, whereas the purity of b -jets increases with w . For each b -tagging algorithm a set of operating points, corresponding to a certain w cut value, are defined and calibrated:

- SV0: $\epsilon_b^{\text{sim}} = 50\%$
- IP3D+SV1: $\epsilon_b^{\text{sim}} = 60\%, \epsilon_b^{\text{sim}} = 70\%, \epsilon_b^{\text{sim}} = 80\%$
- JetFitter: $\epsilon_b^{\text{sim}} = 57\%, \epsilon_b^{\text{sim}} = 60\%, \epsilon_b^{\text{sim}} = 70\%, \epsilon_b^{\text{sim}} = 80\%$
- MV1: $\epsilon_b^{\text{sim}} = 60\%, \epsilon_b^{\text{sim}} = 70\%, \epsilon_b^{\text{sim}} = 75\%, \epsilon_b^{\text{sim}} = 85\%$

where ϵ_b^{sim} is the nominal b -tagging efficiency derived from an inclusive sample of simulated $t\bar{t}$ events.

The mistag rate is measured in data using two methods, both based on an inclusive sample of jets, referred to as the *negativetag* and *sv0mass* methods [33]. The first method uses the invariant mass spectrum of tracks

associated with reconstructed secondary vertices to separate light and heavy-flavour jets, and the other is based on the rate at which secondary vertices with negative decay length, or tracks with negative impact parameter, are present in the data.

Currently, there is no explicit measurement of the c -tag efficiency available in ATLAS. As both the b - and c -tag efficiencies are dominated by decays of long-lived heavy flavour hadrons, they are expected to show a similar behaviour. In general, for physics analyses, it is thus assumed that the scale factor is the same for b - and c -jets. However, to take into account possible deviations from this assumption, the systematic uncertainty for the c -tag efficiency scale factor is inflated by a factor of two, which is considered to be a conservative choice based on simulation studies. In the future, the c -tag efficiency is expected to be measured in dedicated analyses.

Bibliography

- [1] Amos Breskin and Rudiger Voss. *The CERN Large Hadron Collider: Accelerator and Experiments*. CERN, Geneva, 2009.
- [2] ATLAS Collaboration. Luminosity Determination in pp Collisions at $\sqrt{s} = 7$ TeV using the ATLAS Detector in 2011. *ATLAS-CONF-2011-116*, Aug 2011.
- [3] S van der Meer. Calibration of the effective beam height in the ISR. *CERN-ISR-PO-68-31. ISR-PO-68-31*, 1968.
- [4] Aad, G. and others. The ATLAS Experiment at the CERN Large Hadron Collider. CERN, Geneva, 2008.
- [5] G. Aad et al. Charged-particle multiplicities in pp interactions measured with the ATLAS detector at the LHC. *New J.Phys.*, 13:053033, 2011.
- [6] ATLAS Collaboration. Estimating Track Momentum Resolution in Minimum Bias Events using Simulation and K_s in $\sqrt{s} = 900$ GeV collision data. *ATLAS-CONF-2010-009*, 2010.
- [7] ATLAS Collaboration. Tracking Studies for b-tagging with 7 TeV Collision Data with the ATLAS Detector. *ATLAS-CONF-2010-070*, 2010.

- [8] Abat, E. and others. Combined performance studies for electrons at the 2004 ATLAS combined test-beam. *Journal of Instrumentation*, 5(11):P11006, 2010.
- [9] M. Aharrouche et al. Measurement of the response of the atlas liquid argon barrel calorimeter to electrons at the 2004 combined test-beam. *Nuclear Instruments and Methods in Physics Research Section A: Accelerators, Spectrometers, Detectors and Associated Equipment*, 614(3):400 – 432, 2010.
- [10] M. Aharrouche et al. Response uniformity of the atlas liquid argon electromagnetic calorimeter. *Nuclear Instruments and Methods in Physics Research Section A: Accelerators, Spectrometers, Detectors and Associated Equipment*, 582(2):429 – 455, 2007.
- [11] Aharrouche M. and others. Energy linearity and resolution of the ATLAS electromagnetic barrel calorimeter in an electron test-beam. *Nuclear Instruments and Methods in Physics Research Section A: Accelerators, Spectrometers, Detectors and Associated Equipment*, 568(2):601 – 623, 2006.
- [12] M. Cojocaru et al. Hadronic calibration of the atlas liquid argon endcap calorimeter in the pseudorapidity region in beam tests. *Nuclear Instruments and Methods in Physics Research Section A: Accelerators, Spectrometers, Detectors and Associated Equipment*, 531(3):481 – 514, 2004.
- [13] J. Pinfold et al. Performance of the atlas liquid argon endcap calorimeter in the pseudorapidity region in beam tests. *Nuclear Instruments and*

Methods in Physics Research Section A: Accelerators, Spectrometers, Detectors and Associated Equipment, 593(3):324 – 342, 2008.

- [14] Calafiura, P. and Lavrijsen, W. and Leggett, C. and Marino, M. and Quarrie, D. The athena control framework in production, new developments and lessons learned. pages 456–458, 2005.
- [15] ATLAS Collaboration. Performance of Jet Algorithms in the ATLAS Detector. *ATL-PHYS-INT-2010-129*, 2010.
- [16] ATLAS Collaboration. Properties of Jets and Inputs to Jet Reconstruction and Calibration with the ATLAS Detector Using Proton-Proton Collisions at $\sqrt{s} = 7$ TeV. *ATLAS-COM-CONF-2010-055*, 2010.
- [17] W. Lampl et al. Calorimeter Clustering Algorithms: Description and Performance. *ATL-LARG-PUB-2008-002*. *ATL-COM-LARG-2008-003*, Apr 2008.
- [18] ATLAS Collaboration. ATLAS Calorimeter Response to Single Isolated Hadrons and Estimation of the Calorimeter Jet Scale Uncertainty. *ATLAS-CONF-2011-028*, 2011.
- [19] G. Abbiendi et al. Inclusive analysis of the b quark fragmentation function in Z decays at LEP. *Eur.Phys.J.*, C29:463–478, 2003.
- [20] Koya Abe et al. Measurement of the b quark fragmentation function in Z0 decays. *Phys.Rev.*, D65:092006, 2002.
- [21] Andy Buckley, Hendrik Hoeth, Heiko Lacker, Holger Schulz, and Jan Eike von Seggern. Systematic event generator tuning for the LHC. *Eur. Phys. J. C*, 65:331–357, 2010.

- [22] Bowler, M. G. Production of heavy quarks in the string model. *Zeitschrift fur Physik C Particles and Fields*, 11:169–174, 1981. 10.1007/BF01574001.
- [23] T Cornelissen, M Elsing, S Fleischmann, W Liebig, E Moyse, and A Salzburger. Concepts, Design and Implementation of the ATLAS New Tracking (NEWT). *ATL-SOFT-PUB-2007-007. ATL-COM-SOFT-2007-002*, 2007.
- [24] ATLAS Collaboration. Performance of primary vertex reconstruction in proton-proton collisions at $\sqrt{s} = 7$ TeV in the ATLAS experiment. *ATLAS-CONF-2010-069*, 2010.
- [25] J. Neyman and E.S. Pearson. On the Problem of the Most Efficient Tests of Statistical Hypotheses. *Royal Society of London Philosophical Transactions Series A*, 231:289–337, 1933.
- [26] ATLAS Collaboration. Commissioning of the ATLAS high-performance b -tagging algorithms in the 7 TeV collision data. *ATLAS-CONF-2011-102*, 2011.
- [27] ATLAS Collaboration. Performance of Impact Parameter-Based b -tagging Algorithms with the ATLAS Detector using Proton-Proton Collisions at $\sqrt{s} = 7$ TeV. *ATLAS-CONF-2010-091*, 2010.
- [28] V Kostyukhin. Vkalvrt - package for vertex reconstruction in atlas. *ATL-PHYS-2003-031*, Aug 2003.
- [29] ATLAS Collaboration. Performance of the ATLAS Secondary Vertex b -tagging Algorithm in 7 TeV Collision Data. *ATLAS-CONF-2010-042*, 2010.

- [30] ATLAS Collaboration. Calibrating the b-Tag Efficiency and Mistag Rate in 35 pb^{-1} of Data with the ATLAS Detector. *ATLAS-CONF-2011-089*, 2011.
- [31] ATLAS Collaboration. Statistical combination of top quark pair production cross-section measurements using dilepton, single-lepton, and all-hadronic final states at $\sqrt{s} = 7 \text{ TeV}$ with the ATLAS detector. *ATLAS-CONF-2012-024*, Mar 2012.
- [32] ATLAS Collaboration. Measuring the b-tag efficiency in a top-pair sample with 4.7 fb^{-1} data from the ATLAS detector. *ATLAS-CONF-2012-097*, 2012.
- [33] ATLAS Collaboration. Measurement of the Mistag Rate with 5 fb^{-1} of Data Collected by the ATLAS Detector. *ATLAS-CONF-2012-040*, 2012.